Spring 2018

Modeling and control of probe-on-probe dynamics in dual-probe atomic force microscopy

Ayad Al-Ogaidi

Department: Mechanical and Aerospace Engineering

MODELING AND CONTROL OF PROBE-ON-PROBE DYNAMICS IN DUAL-PROBE ATOMIC FORCE MICROSCOPY

by

AYAD JASIM MOHAMMED AL-OGAIDI

A Dissertation

Presented to the Graduate Faculty of the

MISSOURI UNIVERSITY OF SCIENCE AND TECHNOLOGY

In Partial Fulfillment of the Requirements for the Degree

DOCTOR OF PHILOSOPHY

in

MECHANICAL ENGINEERING

2018

Approved by:

Douglas A. Bristow, Advisor
Jagannathan Sarangapani
S.N. Balakrishnan
Robert Landers
Tansel Yucelen

PUBLICATION DISSERTATION OPTION

This dissertation consist of three articles which will submitted for publication as follows and have been formatted in the style used by Missouri University of Science and Technology.

PAPER I: Pages 6-32 are intended for submission to ASME Journal of Dynamic Systems, Measurements and Control.

PAPER II: Pages 33-47 are intended for submission to ASME Journal of Dynamic Systems, Measurements and Control.

PAPER III: Pages 48-62 are intended for submission to IEEE Transaction on Mechatronics.

ABSTRACT

The atomic force microscope (AFM) is a widely used instrument for imaging and direct manipulation of materials and particles at the nanoscale. The AFM uses a probe, which is a microcantilever with a sharp point at the end. Typically, the AFM is constructed with a single probe. The disadvantage of this construction is that it can only be used either for imaging or manipulation in one implementation. An AFM was constructed using two probes, permitting simultaneous imaging and manipulation. A dual-probe AFM (DP-AFM) provides a foundation for feedback controlled manipulation.

Paper I investigates probe-on-probe contact stability and examines the dynamics of probe-on-probe contact. Evaluation of these interactions leads to study the stability of state-dependent switched systems. Uniform ultimate boundedness theorem and sequence nonincreasing condition corollary were employed to show stability of proposed state dependent switched model with DP-AFM application.

Paper II is extending approach-retract curve to characterize probe-on-probe interaction. Universal sensitivity model for probe-on-probe interaction was found. During the retract phase, adhesion occurs between probes. Jump-off-contact deflection between probes was employed for adhesion force calculation.

Paper III represents implementation of Iterative Learning Control on Z-axis nano-stage with stochastic and deterministic noise. The nano stage model was identified using frequency response of the stage. Deterministic and stochastic noise spectrum was identified experimentally. Optimal Q filter and learning filter (L-filter) were designed depending on the deterministic and stochastic noise spectrum. The error norm was experimentally found to be converging for all four ILC algorithms.

ACKNOWLEDGMENTS

I would like to thank my advisor, Dr. Douglas Bristow, for his guidance, support, and mentorship that has shaped me as a professional. His optimism and enthusiasm for the research were a constant encouragement to me. I deeply appreciate his infinite patience and constructive criticism that made this work possible.

I would like to thank my dissertation committee, Dr. Jagannathan Sarangapani, Dr. S.N. Balakrishnan, Dr. Robert Landers, and Dr. Tansel Yucelen, for their useful and insightful comments. Also, I would like to thank Dr. Eric Bohannan for his help with the AFM. Special thanks to my colleagues in the Precision Motion Control Lab, Dr. Muthukumaran Loganathan and Abdulmohsen, for the technical support and sharing their insight about the AFM.

I would like to acknowledge the Higher Committee for Education Development in Iraq (HCED-Iraq) for granting me a scholarship to study at Missouri S&T. Also, I would like to acknowledge the financial support from the National Science Foundation (CMMI-1229701) and the Intelligent Systems Center (ISC) at Missouri S&T.

I would like to extend my thanks to my parents for their love, kindness, and support. Special thanks to my wife for her love, and enduring patience during these years in graduate school. Last but not least, I would like to thank my kids Zain, Anas, Mohammed, and Demah who have been nothing short of amazing.

TABLE OF CONTENTS

LIST OF FIGURES

LIST OF TABLES

1. INTRODUCTION

1.1. ATOMIC FORCE MICROSCOPY

The atomic force microscope (AFM) [1] uses a micro-cantilever with a sharp point at the end to manipulate and sense objects at nano scale. The probe deflection is measured by the optical lever technique [2], where a laser beam focused on the back of the probe is reflected back into a position-sensitive photodetector (PSD). Measuring the displacement of the laser spot on the PSD indicates the deflection measurement. This deflection measurement is regulated by the mean of feedback controller.

One of important capability of the AFM is that it can be used to image biological samples [3], conductors [4], and insulators [5] at different ambient conditions at air [6], liquid [7], and vacuum [8]. The AFM can work at different modes; the most important modes are contact and tapping. At the tapping mode, the probe oscillates at its resonant frequency and the tip softly taps the sample. At the contact mode, the probe will be directly in contact with the sample. The sample image is directly affected by the probe tip condition. For example, using a worn tip [10] will result in a bad image, while using a sharp tip will result in a good image. Using contact mode results in a good image of the sample topography, but it will damage the probe tip and the sample surface, while using tapping mode will result in a good image with minimum damage to the probe and the sample.

Depending on the AFM mode, tip deflection (contact mode) or the RMS of the deflection (tapping mode) is regulated by a mean of feedback control of the z-axis nano stage, and the control action generates the sample topography, as shown in Figure 1.1.

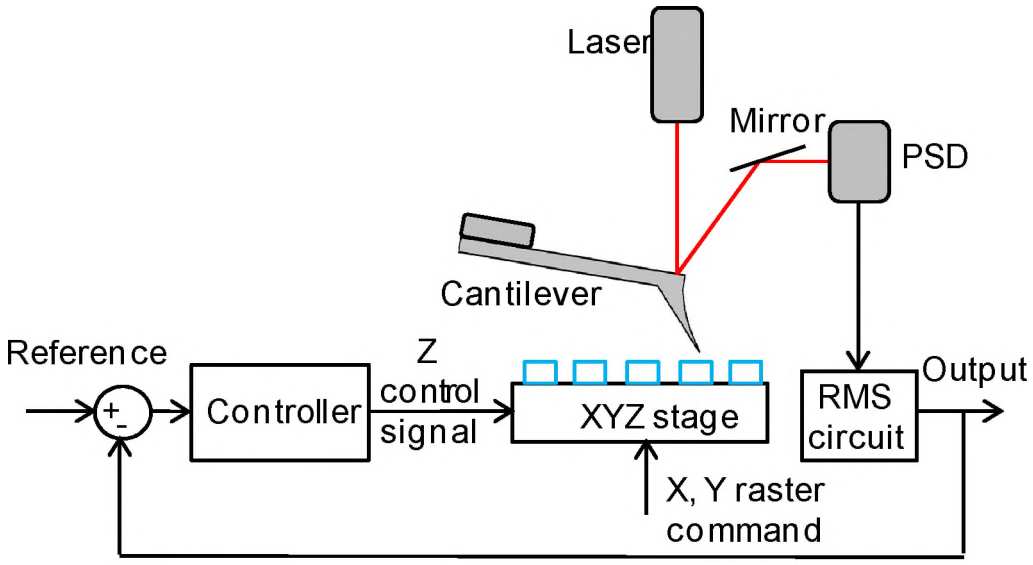

Figure 1.1. Schematic of AFM control loop [11].

1.2. DUAL-PROBE ATOMIC FORCE MICROSCOPY

A typical AFM can only be used either for imaging or manipulation in one implementation, because the probe can only image or manipulate at any given time. For this reason, most of the nano manipulation was implemented in an open loop process due to the lack of the real-time monitoring of the process. This drawback of the AFM motivates the work toward dual-probe AFM (DP-AFM).

An AFM was constructed using two probes, permitting simultaneous imaging and manipulation. A DP-AFM [11] provides a foundation for real-time monitoring and control of a variety of direct manipulation tasks (plowing, pushing/pulling, printing, etc.). Also, it can be used for simultaneous imaging of a different sample's properties, one probe imaging the sample topography and the other imaging another mechanical property. A DP-AFM can be used for picking and placing of nano objects where the

probes work as a nano manipulator. A schematic of the DP-AFM and an actual experimental setup are shown in Figure 1.2.

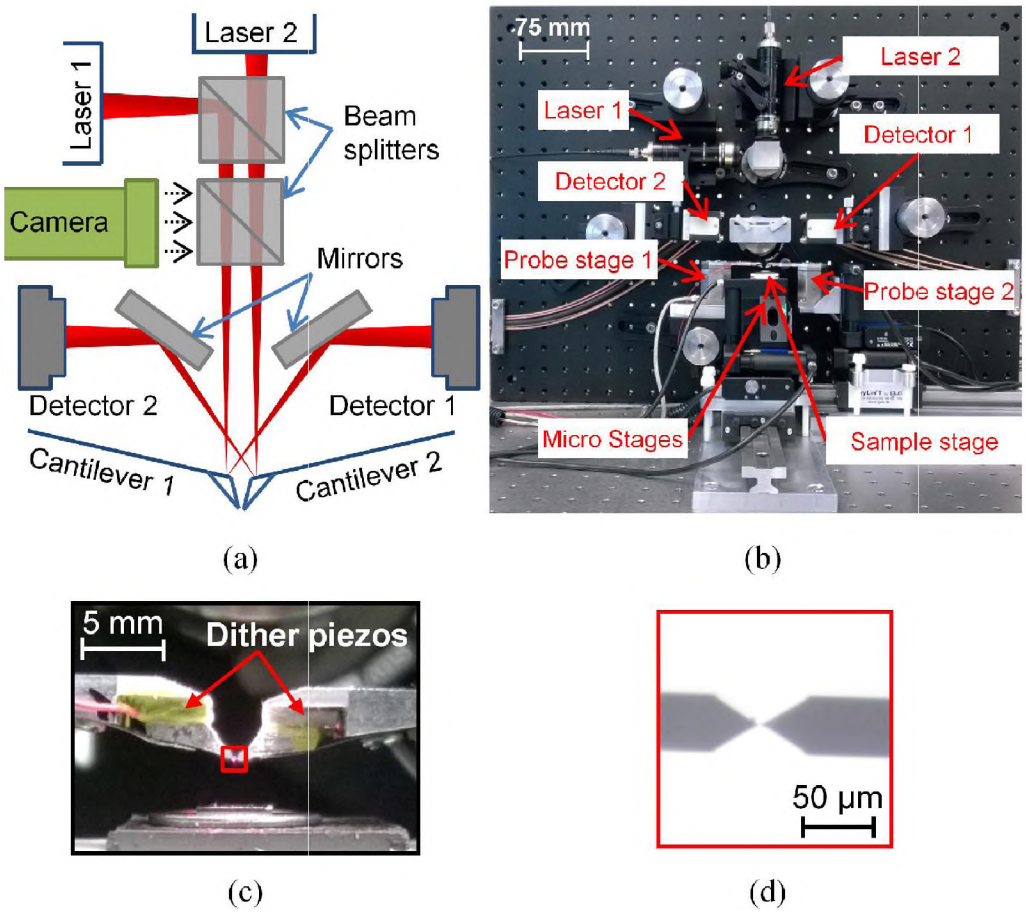

Figure 1.2. (a) Schematic of DP-AFM. (b) Image of the actual DP-AFM setup. (c) Zoomed in image showing the probe holders with dither piezos. (d) Camera view (top view) of the two top visual probes aligned tip-to-tip [11].

1.3. PROBE-ON-PROBE INTERACTION

In DP-AFM, where two probes work simultaneously close to each other, interaction may occur between the probes accidently due to thermal drift [12], or it may occur on purpose when locating one probe with another, or when the two probes are

working as a nano gripper. This interaction opens the question about the probe-on-probe stability. In this work, we will answer a question about probe-on-probe stability and examine the dynamics of probe-on-probe response to characterize stable and unstable probe-on-probe interaction.

When two objects are interacting at nano level, these objects are subject to inter-atomic force. The inter-atomic force can be modeled by the Lennard Jones model. The Lennard Jones model represents a nonlinear model of inter-atomic attractive and repulsive forces. This model can be linearized to a piecewise continuous model [13] with linear attractive and repulsive regions. Evaluation of this interaction model leads to study the stability of switched systems. Stability of switched systems can be established by showing the convergence of the Lyapunov function. The analysis and theory of the DP-AFM interaction will be addressed in detail in Paper I.

On the other hand, the Lennard Jones model did not include the adhesion between atoms, which is a widely known phenomenon of nano objects. The adhesion occurs mainly due to surface tension between the interacting objects. At retract phase, probe tips adhere together until the probes' spring force overcomes the adhesion force, where probes will jump-off-contact (JOC) and separate. Adhesion force can be calculated theoretically by JKR and DMT models. On the other hand, it can be found experimentally from JOC deflection. This will be addressed in Paper II.

1.4. ITERATIVE LEARNING CONTROL

Iterative learning control (ILC) [14]-[16] is a control process used to improve the performance of systems that execute the same operation again and again. A common

example of such system is an industrial robot, that repeats the same task many times over a finite time. ILC requires that the system will be reset to the same initial condition when the iteration is done. ILC employs the tracking error from previous iterations to generate a control signal for the next iteration.

One of the advantages of ILC over other feedforward and feedback controllers is that ILC learns to reject noise and disturbance from propagating through iterations. For instance, feedback controllers react to input and disturbance that cause lag in the system transient response [16]. On the other hand, feedforward controllers can eliminate lag for known reference signals, but not for disturbance [16]. ILC can reject the repeating disturbance by learning from the previous iteration. Also, ILC does not require a reference signal or disturbance to be known; the only requirement is that it should be repeated.

PAPER

I. UNIFORM ULTIMATE BOUNDEDNESS OF PROBE-ON-PROBE DYNAMICS IN DUAL-PROBE ATOMIC FORCE MICROSCOPY

Ayad Al-Ogaidi and Douglas A. Bristow

ABSTRACT

Atomic force microscopy uses a probe with a sharp nano tip attached at the end to sense or manipulate nano objects. Dual probe atomic force microscopy (DP-AFM) uses two probes for simultaneous imaging and manipulation. With dual probes working close to each other, probe-on-probe interaction may occur accidentally (due to thermal drift) or on purpose (by picking and placing a nano object). This work investigates the stability of probe-on-probe interaction in DP-AFM for the case when the 1^{st} probe is the imaging probe and the 2^{nd} probe is the manipulation probe. Uniform ultimate boundedness (UUB) theorem and sequence nonincreasing condition corollary were employed to show the stability of the proposed state-dependent switched model with DP-AFM application.

1. INTRODUCTION

The atomic force microscope (AFM) [1] is a widely used instrument for imaging and direct manipulation of materials and particles at the nanoscale. An AFM uses a micro cantilever with a sharp tip at the end to manipulate or sense a nano object. Typically AFMs have a single probe and perform one task at a time. For instance, a single probe AFM can manipulate a nano object without any monitoring process, so when the

manipulation process is done, AFM will be switched to a sensing mode (imaging mode) to monitor the manipulation process offline. This drawback of single-probe AFM motivates the work toward dual-probe (DP) AFM. In DP-AFM, two probes work simultaneously to perform a real-time manipulation and imaging process.

DP-AFM performs manipulation and sensing processes together, with two probes working close to each other, which can result in these probes interacting with each other accidentally, such as when thermal drift is involved [19], or the interaction may occur on purpose when locating one probe with another [19] or during a picking and placing of a nano object. This interaction opens a question about DP-AFM stability under interaction, this paper will investigate and answer this question.

In this preliminary work, the 1st probe is assumed to be a tapping mode (TM) probe used for the imaging process and the 2nd probe is assumed to be a contact mode (CM) probe used for manipulation. This work investigates probe-on-probe interaction and does not consider probe-sample interaction. Probe interaction is subject to inter-atomic force between the tips of these probes. Intermittent contact between the probes, as when a tapping probe "taps" against the contact probe, motivate a concept of stability of a switched system.

The Lyapunov stability theory represents an essential tool to evaluate stability of a switched system. The stability of switched system can be proven by showing the existence of a common Lyapunov candidate for all subsystems [3]. Many works have investigated the construction of common Lyapunov function of switched system. In [22] [23], a common Lyapunov function is constructed by using Lie algebra. In [24], a common Lyapunov function is constructed for commuting Hurwitz system matrices by

using an iterative procedure. In the absence of a common Lyapunov function, the stability of a switched system will be established with multiple Lyapunov functions. Despite the Lyapunov function showing stability of every subsystem when this subsystem is active, it may diverge when switching between subsystems. To establish the stability of a switched system with multiple Lyapunov functions, a sequence nonincreasing condition [8] will be employed. In [3], [8] and [10] the asymptotic stability of a switched systems is investigated with a sequence nonincreasing condition. For practical systems under driving force or external perturbation, it may be difficult to establish asymptotic stability, and for this reason uniform ultimate boundedness (UUB) will be more practical to demonstrate.

UUB stability of an arbitrary switched system has been investigated in many articles [4-7]. However, not much has been done for a state-dependent switched system. In [5], a switching signal with infinite number of switching is designed to preserve UUB of all subsystems were the switching signal is given as state feedback control signal. In [6], UUB of switched system with arbitrary switching law is guaranteed by using a common Lyapunov function with a sufficient linear inequality condition. While in [7], an algorithm for designing a continuous controller and switching strategy is established to ensure UUB of switched system. In this work, UUB stability of a state-dependent switched system will be investigated for a family of N switched systems. The main contribution of this work is the UUB stability of a family of N-state-dependent switched system with sequence nonincreasing condition and their application to DP-AFM.

This paper is organized as follows. Section 2 presents a theorem for UUB of switched system under the sequence nonincreasing condition. Section 3 presents a state-dependent switched system model for dual- probe interaction. Section 4 proves the UUB

of the DP-AFM. Section 5 presents a simulation results and application of the developed theorems for probe-on-probe interaction. Section 6 presents the conclusions.

2. UUB AND SEQUENCE NONINCREASING CONDITION

One of the sufficient conditions to show stability of a switched system is by finding a common Lyapunov function for all subsystems [3]. However, finding a common Lyapunov function is not easy, yields using a multiple Lyapunov function for the switched system. To establish stability of a switched system with multiple Lyapunov functions, we need to put a restriction on the switching system. UUB stability of every subsystem has to be established and the switching has to be restricted such that for every p^{th} subsystem, Lyapunov function has to be decreased when switching back to the p^{th} subsystem. This is called sequence nonincreasing condition.

Let a system described by

$$\dot{x} = f_{\sigma(t)}(t, x) \tag{1}$$

be a switched system with switching signal $\sigma(t) \in P = \{1, 2, ..., N\}$. Then the following definition and theorem will establish the UUB stability of the switched system.

2.1. DEFINITION [4]

The switched system with switching signal $\sigma(t)$ is uniformly ultimately bounded (UUB) with ultimate bound b if there exist positive constants b and c such that for every $0 \le a \le c$ there is $T = T(a, b)$ such that $\|x(0)\| \le a$ then, $\|x(t)\| \le b$ for $\forall t \ge T$.

2.2. THEOREM 1

Let (1) be a switched system where $\dot{x} = f_p(t,x)$, $p \in P$, is a family of N uniformly ultimately bounded systems, and let V_p, $p \in P$, be a family of N continuously differentiable Lyapunov functions. Let $t_1 < t_2 < t_3$ .... be switching times such that $\sigma(t) = p$ for $t_i \le t < t_{i+1}$, $i = 1, 2, \ldots$, and $\sigma(t_i) \neq \sigma(t_{i+1})$. If the sequence nonincreasing condition,

$$V_p(t_j, x(t_j)) \le V_p(t_i, x(t_i)), \tag{2}$$

for any $j > i$ with $\sigma(t_i) = \sigma(t_j)$ is satisfied, then the switched system is uniformly ultimately bounded. □

Proof of Theorem 1: See appendix.

In this theory, we apply sequence nonincreasing condition to preserve UUB of switched system with multiple Lyapunov function. Also, we propose a corollary to construct Lyapunov function of the subsystem V_p such that it satisfies the sequence nonincreasing condition. V_p constructed such that for every pth subsystem Lyapunov function is decreased when it switch back to the pth subsystem. Also notice that although V_p is UUB during $\sigma(t) = p$, V_p is not necessarily decreasing during $\sigma(t) \neq p$, in such case, the sequence nonincreasing condition ensures stability, as shown in Figure 1.

2.3. COROLLARY 1

Let $\dot{x} = f_p(x,t)$, and let there exist a family of N continuously differentiable functions $\{V_p : p \in P = \{1, 2, \ldots, N\}\}$ such that,

$$\dot{V}_p(t,x) \le -W_3 \le 0, \quad p \in P. \tag{3}$$

Also, at the switching surface, let

$$V_{i+1}(t,x) = V_i(t,x) + \beta_i \tag{4}$$

where $\beta_i > 0$ is a constant and $t_m < t_{m+2(N-1)}$, where t is the switch time and m is the switch number. $\sigma(t_m) = \sigma(t_{m+2(N-1)})$. Assume further that σ satisfies the structural sequence $\sigma(t_m) = p,\ \sigma(t_{m+1}) = p+1,...,\sigma(t_{m+i}) = p+i,\ \sigma(t_{m+i+1}) = p+i-1,...,$ $\sigma(t_{m+2(i-1)}) = p$ for all $i \le N$. Then the switched system satisfies the sequence nonincreasing condition,

$$V_p(t_{m+2(N-1)}, x(t_{m+2(N-1)})) \le V_p(t_m, x(t_m)). \tag{5}$$

Proof of Corollary 1: See appendix.

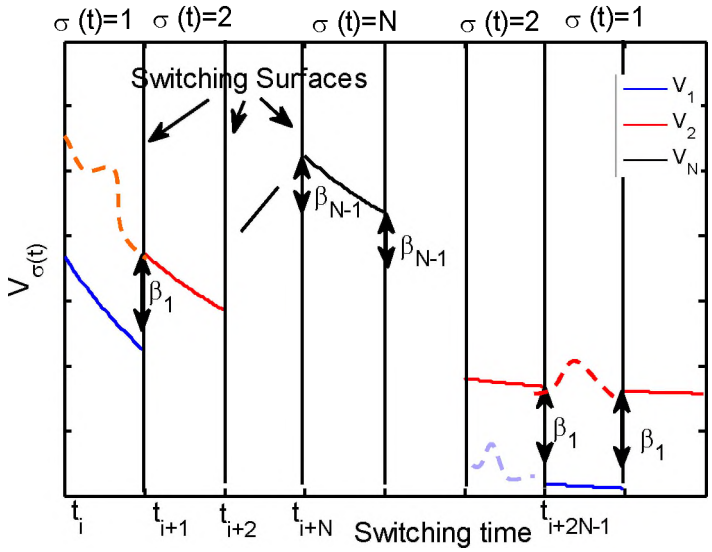

Figure 1. Illustration of the switched Lyapunov function in Corollary 1.

Assume a switching Lyapunov function shown in Figure 1. Although V_i is UUB during $\sigma(t)=i$, V_i is not necessarily decreasing during $\sigma(t)\neq i$, in such case, the sequence nonincreasing condition ensures stability. This is proven by induction (see appendix).

3. A SWITCHED SYSTEM MODEL FOR DP-AFM

Probe dynamics are often modeled as a simple lumped mass-spring-damper system [12] with equivalent mass, spring stiffness, and damping ratio. Consider the DP-AFM shown in Figure 2 with 1st probe is a TM probe and 2nd probe is a CM probe. The DP-AFM can be modeled as the following:

$$m_1\ddot{z}_1(t)+c_1\dot{z}_1(t)+k_1z_1(t)=f_1(z_1(t),t), \tag{6}$$

$$m_2\ddot{z}_2(t)+c_2\dot{z}_2(t)+k_2z_2(t)=f_2(z_2(t)), \tag{7}$$

where m_1,k_1,c_1 are the equivalent mass, spring stiffness, and damping ratio of 1st probe; m_2,k_2,c_2 are the equivalent mass, spring stiffness, and damping ratio of 2nd probe; z_1 and z_2 represent the position of the tip of 1st probe and 2nd probe from the equilibrium position, respectively; and f_1 and f_2 are the forces acting on 1st probe and 2nd probe, respectively. Rewriting (6), (7) yields the following:

$$\ddot{z}_1(t)+\frac{\omega_1}{Q_1}\dot{z}_1(t)+\omega_1^2z_1(t)=\frac{1}{m_1}f_1(z_1(t),t) \tag{8}$$

$$\ddot{z}_2(t)+\frac{\omega_2}{Q_2}\dot{z}_2(t)+\omega_2^2z_2(t)=\frac{1}{m_2}f_2(z_2(t)) \tag{9}$$

where $\omega_1 = \sqrt{k_1/m_1}$, $\omega_2 = \sqrt{k_2/m_2}$ are the natural frequency of 1st probe and 2nd probe, respectively, and $Q_1 = m_1\omega_1/c_1$ and $Q_2 = m_2\omega_2/c_2$ are the quality factor of 1st probe and 2nd probe, respectively.

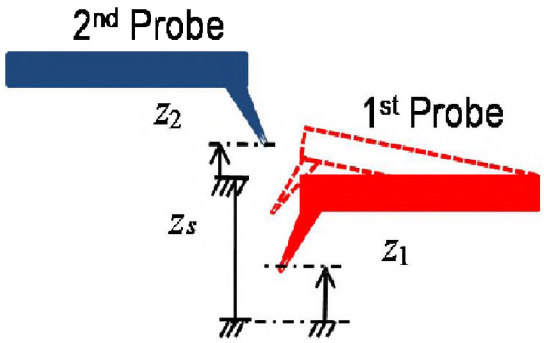

Figure 2. DP-AFM model.

Furthermore, (8) and (9) can be rewritten in terms of the normalized time $\tau = \omega_1 t$, yielding,

$$\ddot{z}_1(\tau) + \frac{1}{Q_1}\dot{z}_1(\tau) + z_1(\tau) = \frac{1}{k_1} f_1(z_1(\tau), \tau) \tag{10}$$

$$\ddot{z}_2(\tau) + \frac{\alpha}{Q_2}\dot{z}_2(\tau) + \alpha^2 z_2(\tau) = \frac{\alpha^2}{k_2} f_2(z_1(\tau), z_2(\tau)), \tag{11}$$

where $\alpha = \omega_2/\omega_1$.

The 1st probe is affected by a driving force, f_{dr}, from the base excitation and the probe-on-probe interaction force, while the 2nd probe is affected by probe-on-probe interaction force. These force are given by,

$$f_1(z_1(\tau), z_2(\tau), \tau) = f_{dr}(\tau) - f_c(z_1(\tau), z_2(\tau)), \tag{12}$$

$$f_2(z_1(\tau), z_2(\tau)) = f_c(z_1(\tau), z_2(\tau)), \tag{13}$$

where $f_{dr}(\tau) = A_0 \sin(\tau)$ is the driving force from base excitation for the 1st probe, A_0 is the amplitude, and $f_c(z_1(\tau), z_2(\tau))$ is probe-on-probe interaction force. Typically, interaction force at the nanoscale is modeled as a nonlinear Lennard-Jones interaction model [13]. This model, shown in Figure 3a, is a nonlinear model with long-range Van-der Waals attractive force originating from charge distribution between interaction atoms [13] and short-range Pauli repulsive force originating from electron cloud overlapping [17]. In the literature, a simplified Lennard-Jones Interaction linear model is used. For instance, [16-17] use a linear regime for attractive and repulsive force. In this work, the Lennard-Jones model will be linearized as a negative spring force at attractive regime and stiff spring force at repulsive regime as shown in Figure 3b, which yields

$$f_c(z_1(\tau), z_2(\tau)) = \begin{cases} 0 & z_1 - z_2 - z_s < b \\ -k_a(z_1 - z_2 - z_s - b) & a > z_1 - z_2 - z_s \geq b \\ -k_a(z_1 - z_2 - z_s - b) + k_c(z_1 - z_2 - z_s - a) & z_1 - z_2 - z_s \geq a \end{cases} \tag{14}$$

where a represents probe inter-atomic distance, b represents the Jump-To-Contact (JTC) distance [21], z_s is the gap between the probes, $z_1 - z_2 - z_s$ is the interaction penetration, $k_a = \dfrac{k_1 k_2}{k_1 + k_2}$ is equivalent attractive stiffness, and k_c approximates the repulsive stiffness. Modeling the linearized interaction force as piecewise continuous with three forcing regions, yields a DP-AFM model as a state-dependent switching system with three subsystems.

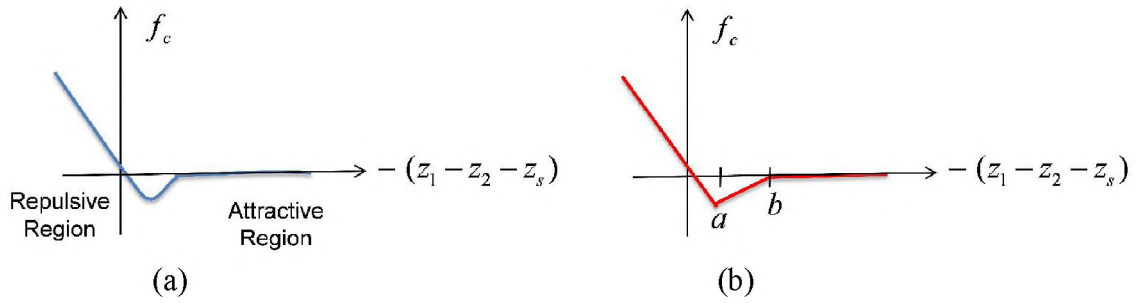

Figure 3. Lennard-Jones interaction model (a) nonlinear model, (b) piecewise continuous linearized model [16]-[17].

To rewrite the previous equations in switched subsystem model, let S_1 be 1st switched subsystem, when $z_1(\tau)-z_2(\tau)-z_s<b$, there is no contact between the probes and the TM probe is at free amplitude. The DP-AFM is modeled as

$$S_1:\begin{cases}\ddot{z}_1(\tau)+\dfrac{1}{Q_1}\dot{z}_1(\tau)+z_1(\tau)=\dfrac{1}{k_1}f_{dr}(\tau),\\ \ddot{z}_2(\tau)+\dfrac{\alpha}{Q_2}\dot{z}_2(\tau)+\alpha^2 z_2(\tau)=0.\end{cases} \tag{15}$$

When the separation between the probes falls between b and a, $a>z_1(\tau)-z_2(\tau)-z_s\geq b$, the attractive force dominates while the repulsive force is negligible, and the DP-AFM modeled as 2nd switched subsystem S_2

$$S_2:\begin{cases}\ddot{z}_1(\tau)+\dfrac{1}{Q_1}\dot{z}_1(\tau)+z_1(\tau)=\dfrac{1}{k_1}f_{dr}(\tau)+\dfrac{k_2}{k_1}(z_1(\tau)-z_2(\tau)-z_s-b),\\ \ddot{z}_2(\tau)+\dfrac{\alpha}{Q_2}\dot{z}_2(\tau)+\alpha^2 z_2(\tau)=-\alpha^2(z_1(\tau)-z_2(\tau)-z_s-b).\end{cases} \tag{16}$$

when the separation between the probes falls below inter-atomic distance, $z_1(\tau)-z_2(\tau)-z_s\geq a$, at this forcing region, the repulsive force experiences a large and

sudden increase due to the overlap between the electron clouds, and the DP-AFM modeled as 3rd switched subsystem S_3

$$S_3 : \begin{cases} \ddot{z}_1(\tau) + \dfrac{\dot{z}_1(\tau)}{Q_1} + z_1(\tau) = \dfrac{f_{dr}(\tau)}{k_1} + \dfrac{k_2}{k_1}(z_1(\tau) - z_2(\tau) - z_s - b) - \dfrac{k_c}{k_1}(z_1(\tau) - z_2(\tau) - z_s - a), \\ \ddot{z}_2(\tau) + \dfrac{\alpha \dot{z}_2(\tau)}{Q_2} + \alpha^2 z_2(\tau) = -\alpha^2(z_1(\tau) - z_2(\tau) - z_s - b) + \dfrac{\alpha^2 k_c}{k_2}(z_1(\tau) - z_2(\tau) - z_s - a). \end{cases} \tag{17}$$

Now, consider a signal $\sigma(\tau)$ that describes the switching such that

$$\sigma(\tau) = \begin{cases} 1, & \tau : z_1(\tau) - z_2(\tau) - z_s < b \\ 2, & \tau : a > z_1(\tau) - z_2(\tau) - z_s \geq b \\ 3, & \tau : z_1(\tau) - z_2(\tau) - z_s \geq a \end{cases} \tag{18}$$

Rewrite the switched system in terms of state space by letting $x_1(\tau) = z_1(\tau)$, $x_2(\tau) = \dot{z}_1(\tau)$, $x_3(\tau) = z_2(\tau)$, $x_4(\tau) = \dot{z}_2(\tau)$, and $x(\tau) = \begin{bmatrix} x_1(\tau) & x_2(\tau) & x_3(\tau) & x_4(\tau) \end{bmatrix}^T$.

Then, the DP-AFM switched system can be represented as

$$\dot{x} = A_{\sigma(t)} x + f_{\sigma(t)} + B_{dr} f_{dr} \tag{19}$$

where

$$A_1 = \begin{bmatrix} 0 & 1 & 0 & 0 \\ -1 & \dfrac{-1}{Q_1} & 0 & 0 \\ 0 & 0 & 0 & 1 \\ 0 & 0 & -\alpha^2 & \dfrac{-\alpha}{Q_2} \end{bmatrix},$$

$$A_2 = \begin{bmatrix} 0 & 1 & 0 & 0 \\ -(1-\frac{k_a}{k_1}) & \frac{-1}{Q_1} & -\frac{k_a}{k_1} & 0 \\ 0 & 0 & 0 & 1 \\ -\frac{\alpha^2 k_a}{k_2} & 0 & -(\alpha^2 - \frac{\alpha^2 k_a}{k_2}) & \frac{-\alpha}{Q_2} \end{bmatrix},$$

$$A_3 = \begin{bmatrix} 0 & 1 & 0 & 0 \\ -(1+\frac{k_c - k_a}{k_1}) & \frac{-1}{Q_1} & \frac{k_c - k_a}{k_1} & 0 \\ 0 & 0 & 0 & 1 \\ \alpha^2 \frac{k_c - k_a}{k_2} & 0 & -(\alpha^2 + \alpha^2 \frac{k_c - k_a}{k_2}) & \frac{-\alpha}{Q_2} \end{bmatrix},$$

$$B_{dr} = \begin{bmatrix} 0 & 1/k_1 & 0 & 0 \end{bmatrix}^T,$$

$$f_1 = \begin{bmatrix} 0 & 0 & 0 & 0 \end{bmatrix}^T,$$

$$f_2 = \begin{bmatrix} 0 & \frac{-k_a}{k_1}(z_s + b) & 0 & \frac{\alpha^2 k_a}{k_2}(z_s + b) \end{bmatrix}^T,$$

$$f_3 = \begin{bmatrix} 0 & \frac{k_c(z_s + a) - k_a(z_s + b)}{k_1} & 0 & \frac{\alpha^2 k_a}{k_2}(z_s + b) - \frac{\alpha^2 k_c(z_s + a)}{k_2} \end{bmatrix}^T.$$

Let the switching surface be defined by

$$x \in \chi_{12},\ \chi_{12} = \{x : x_1 - x_3 - z_s = b\},$$

$$x \in \chi_{23},\ \chi_{23} = \{x : x_1 - x_3 - z_s = a\}.$$

Note that S_1 transition to S_2 when x crosses χ_{12} and S_2 transition to S_3 when x crosses χ_{23} and it is not possible for S_1 to transition to S_3 without passing through S_2.

4. UUB OF SWITCHED SYSTEM

Consider the following Lyapunov functions for DP-AFM:

$$V_1(x) = x^T L_1 x\,, \tag{20}$$

where

$$L_1 = \begin{bmatrix} (\frac{Q_2}{\alpha} + Q_1 + \frac{1}{Q_1}) & 1 & 0 & 0 \\ 1 & \frac{Q_2}{\alpha} + Q_1 & 0 & 0 \\ 0 & 0 & \frac{k_2}{\alpha^2 k_1}(\alpha Q_2 + \alpha^2 Q_1 + \frac{\alpha}{Q_2}) & \frac{k_2}{\alpha^2 k_1} \\ 0 & 0 & \frac{k_2}{\alpha^2 k_1} & \frac{k_2}{\alpha^2 k_1}(\frac{Q_2}{\alpha} + Q_1) \end{bmatrix}, \tag{21}$$

It can be shown that

$$L_1 A_1^T + A_1 L_1 = -H_1\,, \tag{22}$$

where, from (20) and (21),

$$\begin{aligned} V_1 = {} & \frac{Q_2}{\alpha} x_1^2 + \frac{Q_2}{\alpha} x_2^2 + Q_1 x_1^2 + \alpha Q_2 x_3^2 + Q_1 x_3^2 + Q_1 x_4^2 + \frac{k_2}{\alpha^2 k_1}(\sqrt{\frac{\alpha}{Q_2}} x_3 + \sqrt{\frac{Q_2}{\alpha}} x_4)^2 \\ & + (\frac{1}{\sqrt{Q_1}} x_1 + \sqrt{Q_1} x_2)^2 \end{aligned} \tag{23}$$

and

$$\dot{V}_1(x) \le -2x_1^2 - 2\frac{Q_2}{\alpha Q_1} x_2^2 - 2\frac{k_2}{k_1} x_3^2 - 2\frac{k_2 Q_1}{\alpha^2 k_1} x_4^2 + 2\frac{A_0}{k_1} x_1 + 2\frac{A_0}{k_1}(\frac{Q_2}{\alpha} + Q_1) x_2\,. \tag{24}$$

Hence,

$$\dot{V}_1(x) \le 0 \qquad \forall \|x\| \ge \mu_1\,, \tag{25}$$

where,

$$\mu_1 = \frac{1}{4}(\frac{A_0}{k_1})^2 \sqrt{(1+\delta_1)^2 + \left(\frac{\alpha Q_1}{Q_2} + \sqrt{\frac{\alpha Q_1}{Q_2}}\delta_1\right)^2 + \frac{k_1}{k_2}\delta_1^2 + \frac{\alpha^2}{Q_1}\frac{k_1}{k_2}\delta_1^2} \tag{26}$$

and

$$\delta_1 = \sqrt{1 + \frac{\alpha Q_1}{Q_2}(\frac{Q_2}{\alpha} + Q_1)^2}\ .$$

Thus, the 1st subsystem is UUB.

For the 2nd subsystem, recall $a > (x_1 - x_3 - z_s) \geq b$. Let,

$$V_2(x) = V_1(x)\,. \tag{27}$$

and

$$\begin{aligned}\dot{V}_2(x) \leq & -2x_1^2 - 2\frac{Q_2}{\alpha Q_1}x_2^2 - 2\frac{k_2}{k_1}x_3^2 - 2\frac{k_2 Q_1}{\alpha^2 k_1}x_4^2 + 2\frac{A_0}{k_1}x_1 + 2(\frac{Q_2}{\alpha} + Q_1)\frac{A_0}{k_1}x_2 \\ & + 2\frac{k_a}{k_1}(x_1 - x_3 - z_s - b)(x_1 - x_3) + 2\frac{k_a}{k_1}(\frac{Q_2}{\alpha} + Q_1)(x_1 - x_3 - z_s - b)(x_2 - x_4).\end{aligned} \tag{28}$$

Because $a - b > (x_1 - x_3 - z_s - b) \geq 0$, (28) can be bounded by,

$$\begin{aligned}\dot{V}_2(x) \leq & -2x_1^2 - 2\frac{Q_2}{\alpha Q_1}x_2^2 - 2\frac{k_2}{k_1}x_3^2 - 2\frac{k_2 Q_1}{\alpha^2 k_1}x_4^2 + 2\frac{A_0}{k_1}x_1 + 2(\frac{Q_2}{\alpha} + Q_1)\frac{A_0}{k_1}x_2 \\ & + 2\frac{k_a}{k_1}(x_1 - x_3)(a - b) + 2\frac{k_a}{k_1}(\frac{Q_2}{\alpha} + Q_1)(x_2 - x_4)(a - b).\end{aligned}$$

yields,

$$\dot{V}_2(x) \leq 0 \quad \forall \|x\| \geq \mu_2\,, \tag{29}$$

where,

$$\mu_2 = \frac{1}{4}\sqrt{\begin{aligned}&\left(\frac{A_0}{k_1} + \frac{k_a}{k_1}(a-b) + \delta_2\right)^2 + \left(\frac{\alpha Q_1}{Q_2}(\frac{A_0}{k_1} + \frac{k_a}{k_1}(a-b))(\frac{Q_2}{\alpha} + Q_1) + \sqrt{\frac{\alpha Q_1}{Q_2}}\delta_2\right)^2 + \ldots \\ &\ldots + \left(\frac{k_a}{k_2}(a-b) + \sqrt{\frac{k_1}{k_2}}\delta_2\right)^2 + \left(\frac{\alpha^2}{Q_1}\frac{k_a}{k_2}(a-b)(\frac{Q_2}{\alpha} + Q_1) + \sqrt{\frac{\alpha^2}{Q_1}\frac{k_a}{k_2}}\delta_2\right)^2\end{aligned}}$$

and

$$\delta_2 = \sqrt{\begin{array}{l}\frac{1}{2}\left(\frac{A_0}{k_1}+\frac{k_a}{k_1}(a-b)+\right)^2+\frac{1}{2}\frac{\alpha Q_1}{Q_2}\left((\frac{A_0}{k_1}+\frac{k_a}{k_1}(a-b)\right)^2\left(\frac{Q_2}{\alpha}+Q_1\right)^2+\ldots \\ \ldots.+\frac{1}{2}\frac{k_a^2}{k_1k_2}(a-b)^2+\frac{1}{2}\frac{\alpha^2k_1}{k_2}\left(\frac{k_a}{k_1}(a-b)(\frac{Q_2}{\alpha}+Q_1)\right)^2\end{array}}.$$

Thus, the 2nd subsystem is UUB.

Recall the 3rd subsystem, $(x_1 - x_3 - z_s) \geq a$. Let,

$$V_3(x) = V_2(x) + 2\frac{k_c - k_a}{k_1}(\frac{Q_2}{\alpha}+Q_1)(x_1 - x_3 - z_s - a)^2 \tag{30}$$

Notice that, at the switching surface $x \in \chi_{23}$, yields

$$V_3(t,x) = V_2(t,x),\ \forall x \in \chi_{23}. \tag{31}$$

From (27) and (30),

$$\begin{aligned}V_3 = {} & \frac{Q_2}{\alpha}x_1^2+\frac{Q_2}{\alpha}x_2^2+Q_1x_1^2+\alpha Q_2x_3^2+Q_1x_3^2+Q_1x_4^2+\frac{k_2}{\alpha^2k_1}(\sqrt{\frac{\alpha}{Q_2}}x_3+\sqrt{\frac{Q_2}{\alpha}}x_4)^2 \\ & +(\frac{1}{\sqrt{Q_1}}x_1+\sqrt{Q_1}x_2)^2+2\frac{k_c-k_a}{k_1}(\frac{Q_2}{\alpha}+Q_1)(x_1-x_3-z_s-a)^2\end{aligned}$$

and because $(x_1 - x_3 - z_s - a) \geq 0$, $(x_1 - x_3) \geq z_s + a$ and $z_s + a \geq 0$, $\forall\ z_s \geq a$, we have,

$$\begin{aligned}\dot{V}_3(x) \leq {} & -2x_1^2-2\frac{Q_2}{\alpha Q_1}x_2^2-2\frac{k_2}{k_1}x_3^2-2\frac{k_2Q_1}{\alpha^2k_1}x_4^2+2\frac{A_0}{k_1}x_1+2(\frac{Q_2}{\alpha}+Q_1)\frac{A_0}{k_1}x_2 \\ & +2\frac{k_a}{k_1}(x_1-x_3)(a-b)+2\frac{k_a}{k_1}(\frac{Q_2}{\alpha}+Q_1)(x_2-x_4)(a-b) \\ & -2\frac{k_c-k_a}{k_1}(x_1-x_3-z_s-a)(x_1-x_3).\end{aligned} \tag{32}$$

Also notice that $(x_1 - x_3 - z_s - a)(x_1 - x_3) \geq 0$ for $\forall\ z_s \geq a$ yields,

$$\dot{V}_3(x) \leq 0 \qquad \forall \|x\| \geq \mu_3, \tag{33}$$

where,

$$\mu_3 = \mu_2 .$$

Thus, the 3rd subsystem is UUB. Then, (25), (29), and (33) show that the subsystems are UUB. Also, from (27) and (31), $V_2(t,x) = V_1(t,x) \quad \forall x \in \chi_{12}$ and $V_3(t,x) = V_2(t,x)$ $\forall x \in \chi_{23}$. Thus, By Theorem (1) and Corollary (1), the switched system is UUB, ensuring boundedness of probe-on-probe interaction.

While the above UUB results provide a rigorous result for establishing the existence of guaranteed bounds; however, the ultimate bound was very conservative (in order of tens of microns) and using the UUB bound will not distinguish between desired and undesired DP-AFM response.

5. SIMULATION RESULTS

To explore the types of behavior in DP interaction. Consider the following cases, set of parameters listed in Table 1 corresponds to tapping mode probe VIT-P/IR and those set of parameters corresponds to contact mode probe VIT_P_C-A also in table 1, and now look at the response when they interact together.

With slightly different parameters, the simulation results show two different responses: the first response is undesired where probes interaction is large erratic (chaos), and the second response is the desired interaction where both probes interact smoothly.

The first case is shown in Figures 4 and 5. Figure 4 shows the position of two probes and Figure 5 shows the switched system Lyapunov function. In this case, the simulation results show undesired large erratic DP interaction.

The second case is shown in Figure 6 and Figure 7. Figure 6 shows the position of the two probes and Figure 7 shows the switched system Lyapunov function. In this case, the simulation shows that after the first several contacts between the probes, the contact enters into a regular cycle (as evidenced by the periodic switching cycle). This response represents a desired DP interaction where contact mode probe is bouncing smoothly on the tapping mode probe.

We are interested in exploring the critical functional relationships to determine when we are going to get a desired response and when we are going to get undesired erratic response. However, from UUB of switched system, the bound was found to be very conservative, 14 μm for 1st subsystem and 50 μm for 2nd and 3rd subsystems.

Now consider a parameterization relating stiffness and natural frequency of 1st probe with stiffness and natural frequency of 2nd probe. To distinguish between desired and undesired DP interaction, consider the following threshold, the DP interaction is desired when the following threshold is satisfied,

$$\left(\|x_1 + x_3\|_2\right)_{\text{final}} \leq \left(\|x_1 + x_3\|_2\right)_{\text{free amplitude}}.$$

Table 1. Simulated probe parameters.

	TM probe: VIT-P/IR			CM probe: VIT_P_C-A		
	Min.	Max	Nominal	Min.	Max	Nominal
Stiffness(nN/nm)	20	95	50	0.03	1	0.3
Natural frequency (kHz)	200	400	257.7	8	25	14

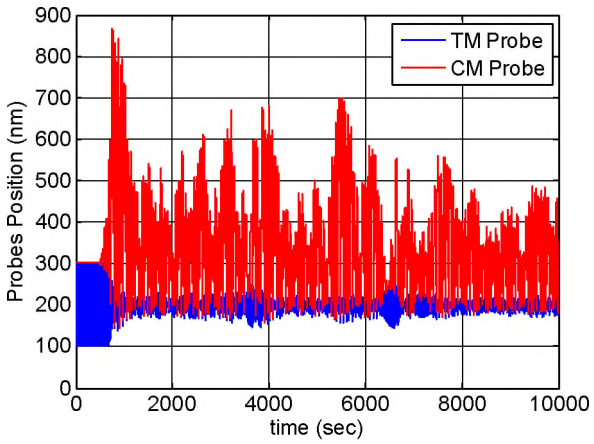

Figure 4. Amplitude of tapping mode and contact mode probes for undesired interaction.

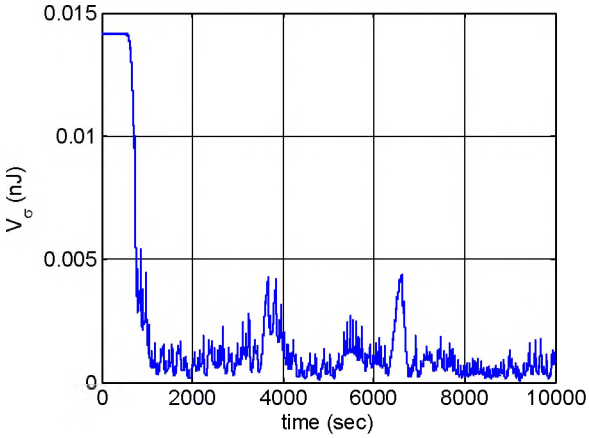

Figure 5. Lyapunov function of switched system for undesired interaction.

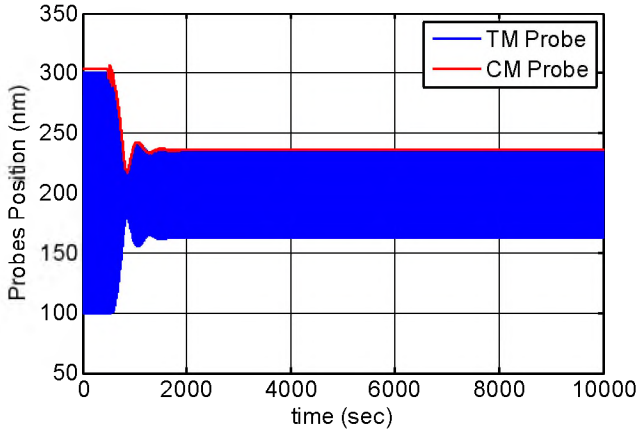

Figure 6. Amplitude of tapping mode and contact mode probes for desired interaction.

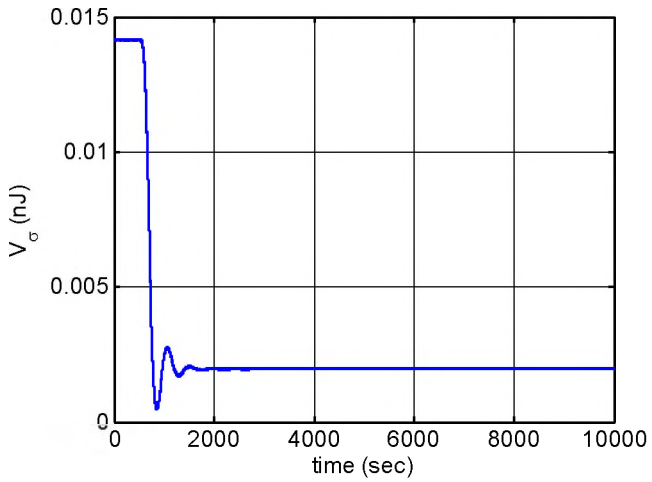

Figure 7. Lyapunov function of switched system for desired interaction.

Using the threshold criteria, DP interaction simulated for different k_2 and f_2 at TM dynamics k_1=50 nN/nm, f_1=257.7 kHz. Figure 8 shows the desired and undesired DP interaction regions. With respect to f_2 increasing k_2 drives the DP interaction toward a desired region, as shown in Figure 8.

On the other hand, Figure 9 shows the desired and undesired DP interaction regions when the DP interaction simulated for different k_1 and f_1, at 2nd probe parameters k_2=0.9 nN/nm, and f_2=14 kHz. Figure 9 shows that the 1st probe parameters' effect is opposite to the 2nd probe effect on DP interaction. With respect to f_1 decreasing k_1 drives the DP interaction toward a desired region, as shown in Figure 9. From these plots we can see that there seems to be a trade off with a critical value between 1st probe and 2nd probe dynamics.

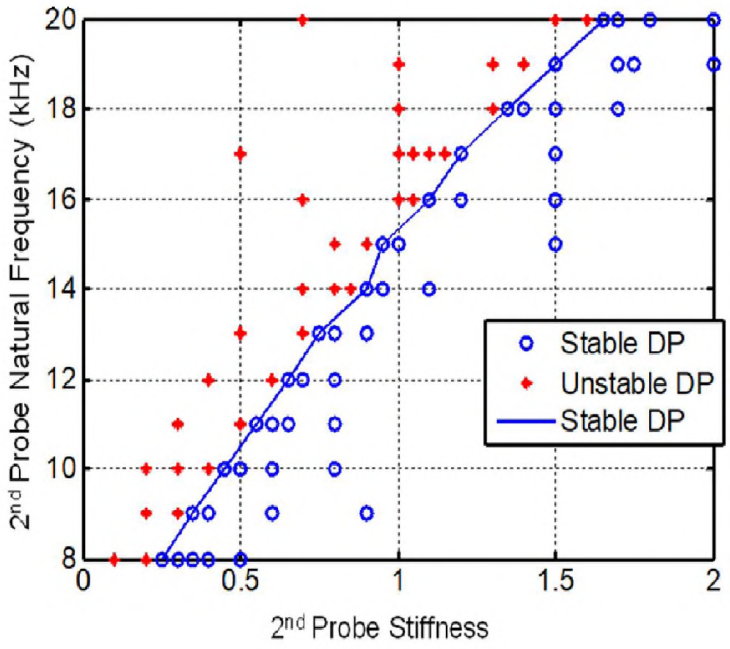

Figure 8. Desired and undesired DP interaction region for different 2nd probe parameters at 1st probe parameters (k_1=50, f_1=257.7 kHz).

6. CONCLUSIONS

The dynamics of probe-on-probe interaction force of DP-AFM were linearized into three regions: no interaction, attraction region, and repulsion region. This linearized interaction force model led to a state-dependent switched system model of three subsystems. Stability of every subsystem was established using Lyapunov stability theorem and proven to be UUB. However, the ultimate bound was found to be conservative. Sequence nonincreasing condition proposed in Corollary (1) was employed to ensure the convergence of every subsystem at the switching surface, which satisfies the convergence of the switched system. The results show that a stable probe-on-probe interaction can be determined for a range of probe dynamics within the operation region.

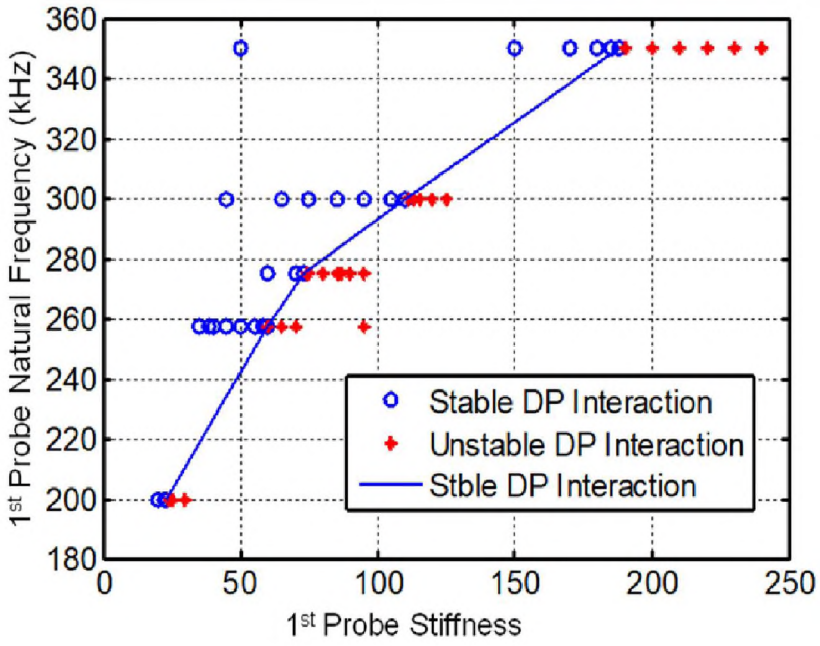

Figure 9. Desired and undesired DP interaction region for different 1st probe parameters at 2nd probe parameters (k_2=0.9, f_2=14 kHz).

APPENDIX

Proof of Theorem 1: Let $\alpha_{l,p}(\|x\|)$ and $\alpha_{u,p}(\|x\|)$ be class κ functions [14] bounds for $V_p(x)$ such that,

$$\alpha_{l,p}(\|x\|) \le V_p(t,x) \le \alpha_{u,p}(\|x\|),\ p \in P. \tag{1}$$

Let $\alpha_1(\|x\|) = \min_{p\in P}\{\alpha_{l,p}(\|x\|)\}$, and $\alpha_2(\|x\|) = \max_{p\in P}\{\alpha_{u,p}(\|x\|)\}$. Then,

$$\alpha_1(\|x\|) \le V_p(t,x) \le \alpha_2(\|x\|),\ p \in P. \tag{2}$$

Because $f_p(t,x)$ are UUB, there exists a $W_p(x)$ positive definite function and μ_p such that,

$$\dot{V}_p(x,t) \le -W_p(x),\ \forall \|x\| \ge \mu_p > 0. \tag{3}$$

Following the approach of [14], we create the following sets. Let $\gamma_t = \{x \in \mathbb{R} \mid \|x\| \le r\}$, for some $r > 0$ and let $U_{p,t} = \{x \in \gamma_t \mid V_p(t,x) \le u\}$ for some $u > 0$. Furthermore, let $L_{p,t} = \{x \in \gamma_t \mid V_p(t,x) \le l\}$ and $R_{p,t} = \{x \in \gamma_t \mid l \le V_p(t,x) \le u\}$ for some $u > l > 0$. Then $L_{p,t} \cup R_{p,t} = U_{p,t}$. Finally, let $q = \min_{\|x\| \ge \mu}\{W_p(x)\}$. Figure A1 shows these sets.

Now, let $x(t_0) \in R_{p,t}$. For $t \ge t_j > t_i \ge t_0$, we have,

$$\dot{V}_p(t,x) \le -q < 0, \text{ and } V_p(t_j, x(t_j)) \le V_p(t_i, x(t_i)),$$

and thus,

$$\begin{aligned} V_p(t,x(t)) &\le V_p(t_j, x(t_j)) \le V_p(t_i, x(t_i)) \\ &\le V_p(t_0, x(t_0)) - q(t - t_0) \\ &\le u - q(t - t_0). \end{aligned} \tag{4}$$

Therefore, we see that the V_p is decreasing in $R_{p,t}$ and any initial condition starting at $R_{p,t}$ will enter to $L_{p,t}$ within a finite time[14]. Also,

$$\dot{V}_p \le -W_p(x) \le -\alpha_{3,p}(\|x\|) \le -\alpha_{3,p}(\alpha_2^{-1}(V_p)) \triangleq -\alpha_{4,p}(V_p)$$

where $\alpha_{3,p}$ and $\alpha_{4,p}$ are class κ functions. Then [14] there is a class κ function σ such that

$$V_p(t,x(t)) \le \sigma(V_p(t_0, x(t_0)), (t - t_0)), \ \forall t \in [t_0, t_0 + T].$$

Defining $\beta(r,s) = \alpha_1^{-1}(\sigma(\alpha_2(r), s)$, then the ultimate bound is

$$\|x(t)\| \le \beta(\|x(t_0)\|, t - t_0), \ \forall t \in [t_0, t_0 + T].$$

Now, for the case when the $x(t_0) \in L_{p,t}$, from (2) we have,

$$\alpha_1(\|x\|) \le V_p(t,x) \le \alpha_2(\|x\|) \le \alpha_2(\mu_p).$$

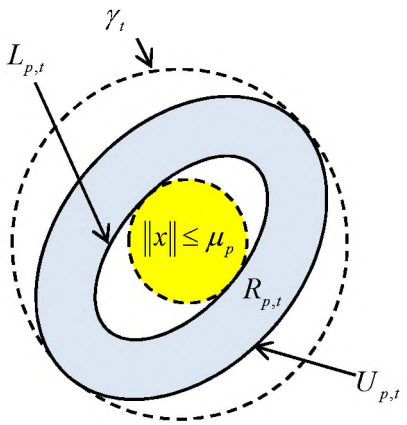

Figure A1. Illustration of the sets γ_t, $U_{p,t}$, $R_{p,t}$ and $L_{p,t}$.

Now, select $l = \alpha_2(\mu_p)$ and thus, $V_p(t,x) \le l$. Also, $\alpha_1(\|x\|) \le \alpha_2(\mu_p)$, so $\|x\| \le \alpha_1^{-1}(\alpha_2(\mu_p))$, $\forall t \ge t_0 + T$. This completes the proof.

Proof of Corollary 1: proof by induction.

First, the corollary has to be valid for N=2, (pair of subsystems), and can be proven as follows. Recall (3), we have, $V_1(t_1,x) \le V_1(t_0,x)$ and thus from (4),

$$V_2(t_2,x) = V_1(t_2,x) + \beta \le V_1(t_1,x) + \beta = V_2(t_1,x). \tag{5}$$

Furthermore,

$$V_1(t_3,x) = V_2(t_3,x) - \beta \le V_2(t_2,x) - \beta = V_1(t_2,x) \tag{6}$$

because $V_2(t_3,x) \le V_2(t_2,x)$. Therefore,

$$V_1(t_2,x) \le V_1(t_0,x) \tag{7}$$

and

$$V_2(t_3,x) \le V_2(t_1,x). \tag{8}$$

Second, the corollary has to be valid for N subsystems, and this could be proved as follow. For N subsystems, from (3), and (4), yields

$$
\begin{aligned}
V_1(t_{2(N-1)+1}) &\le V_2(t_{2(N-1)}) - \beta_1 \le V_3(t_{2(N-1)-1}) - \beta_1 - \beta_2 \le \cdots \\
&\le V_{N-1}(t_{(N+1)}) + \beta_{N-1} - \sum_{j=1}^{N-1}\beta_j \le V_N(t_N) - \sum_{j=1}^{N-1}\beta_j \\
&\le V_{N-1}(t_{(N-1)}) + \beta_{N-1} - \sum_{j=1}^{N-1}\beta_j \le \cdots \le V_3(t_3) - \beta_1 - \beta_2 \le V_2(t_2) - \beta_1 \le V_1(t_1)
\end{aligned} \tag{9}
$$

$$
\begin{aligned}
V_2(t_{2(N-1)+2}) &\le V_1(t_{2(N-1)+1}) + \sum_{j=1}^{N-1}\beta_j - \sum_{j=2}^{N-1}\beta_j \le V_2(t_{2(N-1)}) \le V_3(t_{2(N-1)-1}) + \sum_{j=3}^{N-1}\beta_j - \sum_{j=2}^{N-1}\beta_j \\
&\le \cdots \le V_{N-1}(t_{(N+1)}) + \sum_{j=N-1}^{N-1}\beta_{N-1} - \sum_{j=2}^{N-1}\beta_j \le V_N(t_N) - \sum_{j=2}^{N-1}\beta_j \\
&\le V_{N-1}(t_{(N-1)}) + \sum_{j=N-1}^{N-1}\beta_{N-1} - \sum_{j=2}^{N-1}\beta_j \le \cdots \le V_3(t_3) + \sum_{j=3}^{N-1}\beta_j - \sum_{j=2}^{N-1}\beta_j \le V_2(t_2)
\end{aligned} \tag{10}
$$

$$
\begin{aligned}
V_3(t_{2(N-1)+3}) &\le V_2(t_{2(N-1)+2}) + \sum_{j=2}^{N-1}\beta_j - \sum_{j=3}^{N-1}\beta_j \le V_1(t_{2(N-1)+1}) + \sum_{j=1}^{N-1}\beta_j - \sum_{j=3}^{N-1}\beta_j \\
&\le V_2(t_{2(N-1)}) + \sum_{j=2}^{N-1}\beta_j - \sum_{j=3}^{N-1}\beta_j \le \cdots \ \cdots \le V_{N-1}(t_{(N+1)}) + \sum_{j=N-1}^{N-1}\beta_j - \sum_{j=3}^{N-1}\beta_j \\
&\le V_N(t_N) - \sum_{j=3}^{N-1}\beta_j \le V_{N-1}(t_{(N-1)}) + \sum_{j=N-1}^{N-1}\beta_j - \sum_{j=3}^{N-1}\beta_j \le \cdots \\
&\cdots \le V_4(t_4) + \sum_{j=4}^{N-1}\beta_4 - \sum_{j=3}^{N-1}\beta_j \le V_3(t_3)
\end{aligned} \tag{11}
$$

$$\vdots$$

$$
\begin{aligned}
V_N(t_{2(N-1)+N}) &\le V_{N-1}(t_{2(N-1)+N-1}) + \sum_{j=N-1}^{N-1}\beta_j \le V_{N-2}(t_{2(N-1)+N-2}) + \sum_{j=N-2}^{N-1}\beta_j \le \cdots \\
&\cdots \le V_2(t_{2(N-1)+2}) + \sum_{j=2}^{N-1}\beta_j \le V_1(t_{2(N-1)+1}) + \sum_{j=1}^{N-1}\beta_j \le V_2(t_{2(N-1)}) + \sum_{j=2}^{N-1}\beta_j \le \cdots \\
&\cdots \le V_{N-2}(t_{2(N-1)+N+2}) + \sum_{j=N-2}^{N-1}\beta_j \le V_{N-1}(t_{(N+1)}) + \sum_{j=N-1}^{N-1}\beta_j \le V_N(t_N)
\end{aligned} \tag{12}
$$

From (3) and (9), (10), (11), and (12), yields,

$$V_1(t_{2(N-1)+1}) \le V_1(t_1) \ \text{ and } \ V_1(t_1) \le V_1(t_0)$$

$$V_2(t_{2(N-1)+2}) \le V_2(t_2) \ \text{ and } \ V_2(t_2) \le V_2(t_1)$$

$$V_3(t_{2(N-1)+3}) \le V_3(t_3) \text{ and } V_3(t_3) \le V_3(t_2)$$

$$\vdots$$

$$V_i(t_{2(N-1)+i}) \le V_i(t_i) \text{ and } V_i(t_i) \le V_i(t_{i-1})$$

Now, assume

$$V_1(t_{m+1}) \le V_1(t_{m-2(N-1)+1}) \tag{13}$$

$$V_2(t_{m+2}) \le V_2(t_{m-2(N-1)+2}) \tag{14}$$

$$V_3(t_{m+3}) \le V_3(t_{m-2(N-1)+3}) \tag{15}$$

$$\vdots$$

$$V_N(t_{m+N}) \le V_N(t_{m-2(N-1)+N}) \tag{16}$$

Then, using a similar argument as in (13) to (16),

$$V_1(t_{m+2(N-1)+1}) \le V_1(t_{m+1}) \tag{17}$$

$$V_2(t_{m+2(N-1)+2}) \le V_2(t_{m+2}) \tag{18}$$

$$V_3(t_{m+2(N-1)+3}) \le V_3(t_{m+3}) \tag{19}$$

$$\vdots$$

$$V_N(t_{m+2(N-1)+N}) \le V_N(t_{m+N}) \tag{20}$$

Thus, by induction, the sequence nonincreasing condition is satisfied. □

ACKNOWLEDGEMENTS

This work is supported by the National Science Foundation, CMMI-1229701.

REFERENCES

[1] Binnig, G., Quate, C., and Gerber C., "Atomic Force Microscope," *Physical Review Letters*, Vol. 56(9), pp. 930-933, 1986.

[2] Tsunemi, E., et. al., "Development of Multi-Environment Dual-Probe Atomic Force Microscopy System Using Optical Beam Deflection Sensors with Vertically Incident Laser Beams," Review of Scientific Instruments, Vol. 84(8), pp. 083701: 1-7, 2013.

[3] Liberzon, D., "Switching in System and Control," Boston, Birkäuser, 2003.

[4] Zhang, L., Chen, Y., Sun, Z., Mastorakis, N. and Alexsandrov, A., "Uniformly Ultimate Boundedness Control for Switched Linear Systems with Parameter Uncertainties," American Control Conference, Seattle, Washington, pp. 3971-3974, Jun. 11-13, 2008.

[5] Lin, H., and Antsaklis, P., "Characterizing Uniformly Ultimately Bounded Switched Signal for Uncertain Switched Linear Systems," *Proceeding of the 46th IEEE Conference on Decision and Control,* New Orleans, LA, pp. 6286-6291, Dec. 12-14, 2007.

[6] Aleksandrov, A., Chen, Y., Platonov, A., and Zhang, L., "Stability analysis for class of switched Nonlinear Systems," Automatica 47(10), pp. 2286-2291, 2011.

[7] Zhang, X., and Fan Y., "An Algorithm of Uniform Ultimate Boundedness for Switched Linear Systems," *IEEE SMC Conference Proceedings*, USA, pp. 166-170, Oct. 5-8, 2003.

[8] Branicky, M., "Stability of Switched and Hybrid Systems," *Proceedings of the 33rd IEEE Conference on Decision and Control*, Lake Buena Vista, Florida, Vol. 4, pp. 3498- 3503, Dec. 14-16, 1994.

[9] Liu, J., Liu, X., and Xie, W., "Uniform Stability of Switched Nonlinear Systems," *Nonlinear Analysis: Hybrid Systems*, Vol. 3(4), pp. 441- 454, 2009.

[10] Branicky, M., "Multiple Lyapunov Function and Other Analysis Tools for Switched and Hybrid Systems," *IEEE Transaction on Automatic Control*, Vol. 43(4), pp. 475-482, Apr. 1998.

[11] Peleties, P., and DeCarlo, R., "Asymptotic Stability of m-Switched Systems Using Lyapunov-Like Functions," *American Control Conference*, Boston, MA, pp. 1679-1684, Jun. 26-28, 1991.

[12] Eslami, S., and Jalili, N., "A comprehensive modeling and vibration analysis of AFM microcantilevers subjected to nonlinear tip-sample interaction forces" Ultramicroscopy, Vol. 117, pp. 31– 45, June 2012.

[13] Israelachvili, J., "Intermolecular and Surface Forces," Boston, MA, Academic Press, 1985.

[14] Khalil, H., "Nonlinear Systems," Third Edition, New Jersey, Prentice Hall, Upper Saddle River, pp. 675, 2001.

[15] García, R. and San Paulo, A., "Attractive and repulsive tip-sample interaction regimes in tapping-mode atomic force microscopy" *Phys. Rev.* B 60, 4961, August 1999.

[16] Dankowicz, H., Zhao, X., and Misra, S., "Near-Grazing Dynamics in Tapping Mode Atomic Force Microscopy," *International Journal of Non-Linear Mechanics*, V. 42, Issue 4, pp 697-709, May 2007.

[17] Dankowicz, H., "Nonlinear dynamics as an essential tool for non-destructive characterization of soft nanostructures using tapping-mode atomic force microscopy," *Phil.* Trans. R. Soc. December 2006. DOI: 10.1098/rsta.2006.1907

[18] Rützel, S., Lee, S., and Raman, A., "Nonlinear Dynamics of Atomic-Force-Microscope Probes Driven in Lennard-Jones Potentials," *Mathematical, Physical and Engineering Sciences*, Vol. 459, No. 2036, pp. 1925-1948, Aug. 8, 2003.

[19] Al-Ogaidi, A., and Bristow, D., "Uniform Ultimate Boundedness of Probe-to-Probe Dynamics in Dual Probes Atomics Force Microscopy," *Proceedings of ASME 2014 Dynamic Systems and Control Conference*, San Antonio, Texas, Oct. 22-24, 2014.

[20] Loganathan, M., Al-Ogaidi, A., and Bristow, D., "Design and Control of Dual-Probes Atomic Force Microscope" IEEE/ASME Transaction on Mechatronics, Vol. 23 Issue 1, pp 424-433 Feb. 2018.

II. STATICS OF PROBE-ON-PROBE INTERACTION IN DUAL-PROBE ATOMIC FORCE MICROSCOPY

Ayad Al-Ogaidi and Douglas A Bristow

ABSTRACT

This work characterizes probe-on-probe interactions, where the 1st probe is a soft probe (typically used for manipulation) and the 2nd probe is stiff probe (typically used for imaging). An approach-retract curve, a common method to characterize probe-sample interaction, is extended to characterize probe-on-probe interaction. An approach-retract curve could be divided into different zones based on interaction. At the approach phase, these zones are no-contact, transient, and deflection zone, while at the retract phase these zones are deflection, adhesion, transient, and no-contact zone. At the adhesion zone, where the probes adhere together, the adhesion force is calculated from jump of contact (JOC) deflection between probes. A universal sensitivity model for probe-on-probe interaction was found to relate probe-sample sensitivity with probe-on-probe sensitivity. Experimental validation demonstrated a model error at less than 4%. The 2nd probe natural frequency was modeled and experimentally measured before and during adhesion. The results showed that 2nd probe natural frequency was reduced due to the increase of the mass due to adhesion. The error between the modeled and experimental natural frequency at adhesion was found to be 2%.

1. INTRODUCTION

The atomic force microscope (AFM) [1] is a widely used instrument for imaging and direct manipulation of materials and particles at the nanoscale. An AFM use a micro cantilever with a sharp tip at the end to manipulate or sense a nano object. A typical AFM with a single probe perform one task at a time. For instance, a single probe AFM manipulates a nano object without any monitoring process, so when the manipulation process is done, the AFM will be switched to a sensing mode (imaging mode) to monitor the manipulation process offline. This drawback of a single probe AFM motivates the work toward dual-probe (DP) AFM. In DP-AFM, two probes work simultaneously to perform a real-time manipulation and imaging process.

DP-AFM with two probes working close to each other led to the fact that these probes may interact to each other accidentally, for example when thermal drift was involved [2], the contact may also occur on purpose, for example, picking and placing a nano object in nano manipulation.

This paper is organized as follows. Section 2 presents probe-sample interaction and experimental measurements of probe sensitivity from probe-sample approach-retract curve. Section 3 presents probe-on-probe interaction where a universal sensitivity model validated with the probe-on-probe experimental measurements from a probe-on-probe approach-retract curve. Section 4 presents experimental measurements of the probe-on-probe adhesion force from the jump of contact (JOC) deflection between probes. Section 5 presents probe stiffness calculated by a frequency scaling method where probe natural frequency experimentally measured by frequency sweeping method. Section 6 presents the conclusions of the probe-on-probe interaction.

2. PROBE-SAMPLE APPROACH-RETRACT CURVE

An approach-retract curve [3] is a common method to characterize probe-sample interaction. A probe starts far away from the sample, moves toward a sample until interaction occurs for a certain distance, then the probe retracts back to the original position.

An approach-retract curve could be divided into different zones based on interactions as shown in Figure 1a. At the approach phase, these zones are no-contact (a-b), transient (b-c), and deflection zone (c-d), while at the retract phase these zones are deflection (d-e), adhesion (e-f), transient (f-g), and no-contact zone (f-g).

At region (a-b), there is no contact between the probe and sample. When the probe comes closer to the sample, the probe is affected by the inter-atomic attraction force. When this force exceeds probe stiffness, the probe jumps-to-contact (JTC) with the sample at the transient region (b-c). At region (c-d), the probe deflects due to approaching the sample. When the probe reaches (d) it will retract back. During retraction, the probe is still at the deflection zone (d-e) where point (e) represents zero deflection point. After this point, the probe is at the adhesion zone (e-f) where the probe adheres to the sample until the probe stiffness overcomes the adhesion force. Then, the probe will jump-off-contact (JOC) at the transient region (f-g).

In DP-AFM [4] [5], the probe-sample approach retract curve is implemented for both probe separately to characterize 1^{st} probe-sample sensitivity and 2^{nd} probe-sample sensitivity. The 1^{st} probe-sample approach retract curve was implemented by moving the 1^{st} probe into a silicon sample. In the same way, 2^{nd} probe-sample approach retract

curve was implemented by moving the 2nd probe into the same silicon sample. Probe sensitivity could be found by

$$V_C = a_1 \delta_C$$

yields,

$$a_1 = \frac{\partial V_C}{\partial \delta_C} \tag{1}$$

$$V_T = a_2 \delta_T$$

yields,

$$a_2 = \frac{\partial V_T}{\partial \delta_T} \tag{2}$$

where V_C is 1st photo detector voltage (mV), δ_C is the 1st probe deflection in (nm), a_1 is the 1st probe sensitivity, V_T is the 2nd photo detector voltage (mV), δ_T is 2nd probe deflection in (nm), and a_2 is the 2nd probe sensitivity. Figure 1b shows experimental result of probe-sample approach-retract curve of 1st probe, where a silicon contact mode probe (VIT-P/IR) interacted with silicon calibration sample (HS-20MG).

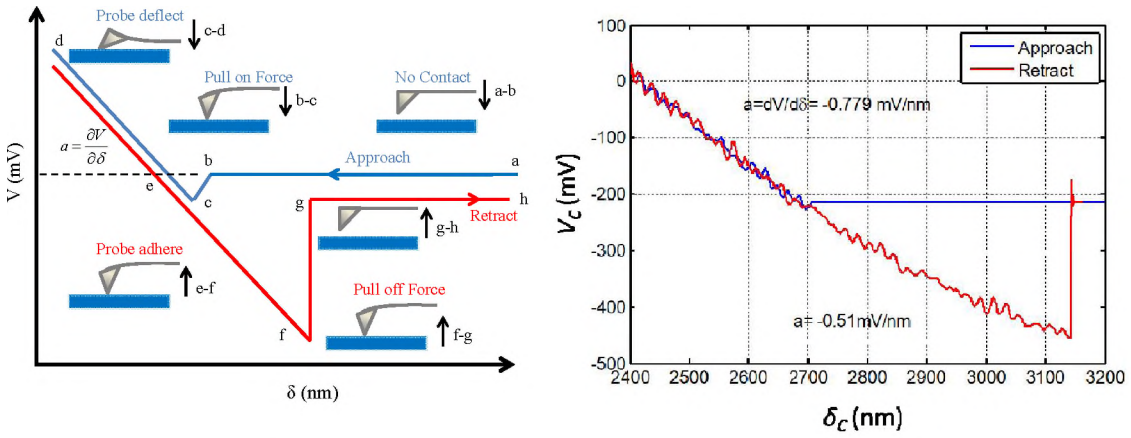

(a) (b)

Figure 1. (a) Schematic of probe-sample approach-retract curve. (b) Experimental of probe-sample approach-retract curve of 1st probe.

3. PROBE-ON-PROBE APPROACH-RETRACT CURVE

The approach-retract curve is extended toward the probe-on-probe interaction. In this preliminary work, consider only probe-on-probe interaction and do not consider the sample interaction with either probe. Consider the probe-on-probe interaction schematic shown in Figure 2a and 2b , where the 1st probe interacts with the 2nd probe instead of interacting with the sample.

In the probe-on-probe approach-retract curve, the 1st probe and 2nd probe approach-retract shows opposite deflection directions as shown in Figure 2a and 2b. However, the approach-retract curve could be divided into no-contact (a-b), transient (b-c), and deflection zone (c-d) in the approach phase, while at the retract phase these zones are deflection (d-e), adhesion (e-f), transient (f-g), and no-contact zone (f-g).

In the probe-on-probe adhesion zone, probe sensitivity relative to each other will be modeled within universal sensitivity model for probe-on probe interaction. Furthermore, probe natural frequency will be changed due to adhesion.

From the transient zone (f-g), adhesion force could be measured experimentally by measuring jump-off-contact (JOC) deflection. This adhesion force plays a big role in nano-manipulation processes.

3.1. EXPERIMENTAL RESULTS: PROBE-ON-PROBE APPROACH-RETRACT CURVE

Figure 3a shows the experimental probe-on-probe approach retract for the 1st probe, while Figure 3b shows the experimental probe-on-probe approach retract of the 2nd probes when the 1st probe base moves for 800 nm at 40 nm/sec.

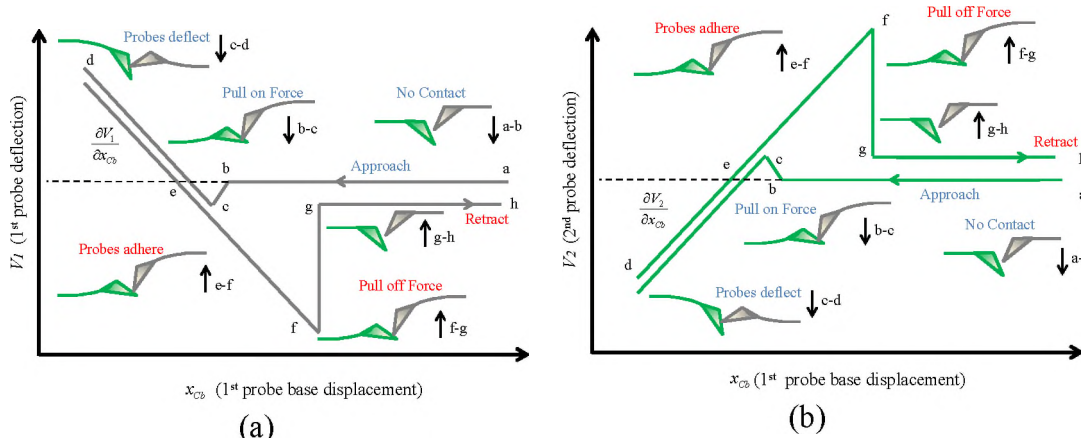

Figure 2. (a) Schematic of probe-on-probe approach-retract curve of 1st probe. (b) Schematic of probe-on-probe approach-retract curve of 2nd probe.

4. PROBE-ON-PROBE SENSITIVITY MODEL

In the probe-on-probe adhesion zone, the probes deflect relative to each other. This changes the probe sensitivity from probe-sample sensitivity. The probe-on-probe sensitivity will be modeled within the universal sensitivity model.

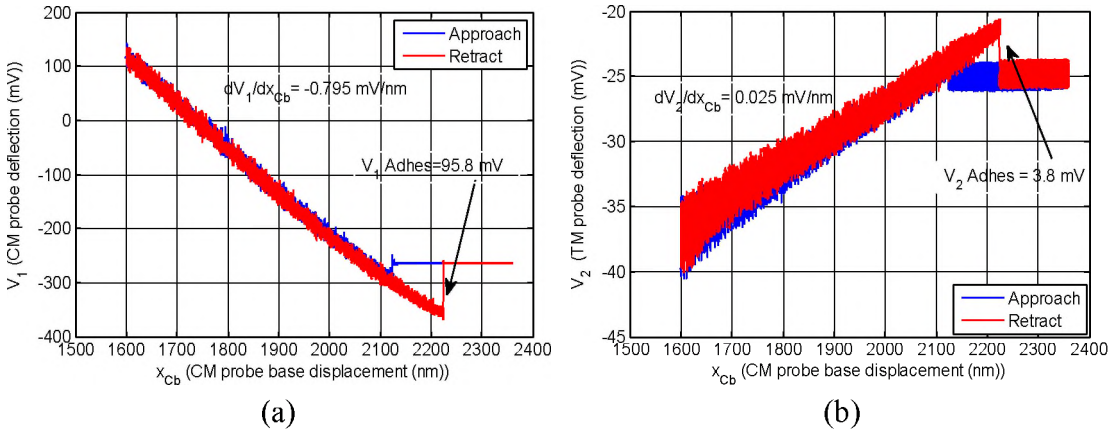

Figure 3. (a) Experimental 1st probe-on-probe approach-retract curve. (b) Experimental 2nd probe-on-probe approach-retract curve.

At the adhesion zone, shown in Figure 4, the DP-AFM could be represented as two springs in a series, as shown in Figure 5, with moving the 1st probe base modeled by,

$$k_C(x_{Cb} - x_P) = k_T x_P \tag{3}$$

where k_C represents 1st probe stiffness, k_T represents 2nd probe stiffness, x_{Cb} represents moving 1st probe base position, and x_P represents probe-on-probe position at adhesion. From (3),

$$x_P = \frac{k_C}{k_C + k_T} x_{Cb} . \tag{4}$$

Also from the probe sensitivity equation,

$$V_1 = a_1(x_{Cb} - x_P) \tag{5}$$

$$V_2 = a_2 x_P \tag{6}$$

Substituting (4) in (6) yields

$$V_2 = a_2 \frac{k_C}{k_C + k_T} x_{Cb} . \tag{7}$$

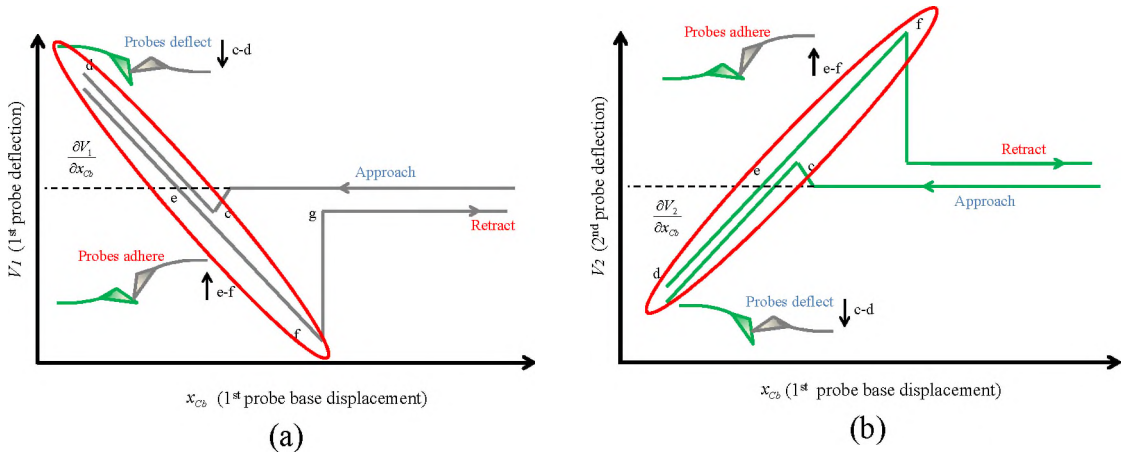

Figure 4. (a) 1st probe-on-probe adhesion zone. (b) 2nd probe-on-probe adhesion zone.

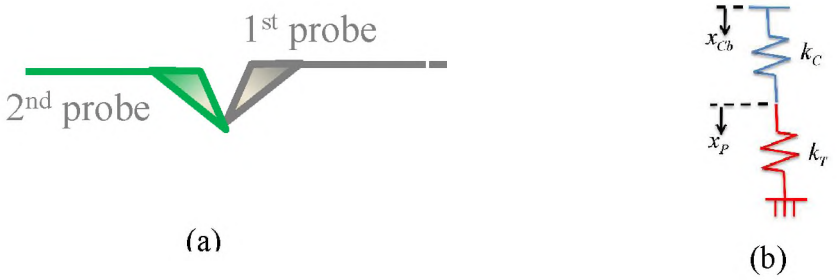

Figure 5. (a) Schematic of two probes at adhesion. (b) At adhesion, probe-on-probe as two springs in series.

Taking a derivate of V_2 with respect to x_{Cb} yields

$$\frac{\partial V_2}{\partial x_{Cb}} = a_2 \frac{k_C}{k_C + k_T}. \tag{8}$$

Also, substitutig (4) in (5) yields

$$V_1 = a_1 \left(1 - \frac{k_C}{k_C + k_T}\right) x_{Cb}. \tag{9}$$

Taking a derivate of V_1 with respect to x_{Cb} yields

$$\frac{\partial V_1}{\partial x_{Cb}} = a_1 \left(1 - \frac{k_C}{k_C + k_T}\right) \tag{10}$$

$$\frac{1}{a_1}\frac{\partial V_1}{\partial x_{Cb}} = 1 - \frac{k_C}{k_C + k_T}. \tag{11}$$

Substituting (8) in (11) yields

$$\frac{1}{a_1}\frac{\partial V_1}{\partial x_{Cb}} = 1 - \frac{1}{a_2}\frac{\partial V_2}{\partial x_{Cb}}. \tag{12}$$

Rewriting (12) yields

$$\frac{1}{a_1}\frac{\partial V_1}{\partial x_{Cb}} + \frac{1}{a_2}\frac{\partial V_2}{\partial x_{Cb}} = 1. \tag{13}$$

Substituting (1) and (2) in (13), and rewriting (13) yields

$$\frac{\partial \delta_C}{\partial x_{Cb}} \frac{\partial V_1}{\partial V_C} + \frac{\partial \delta_T}{\partial x_{Cb}} \frac{\partial V_2}{\partial V_T} = 1. \tag{14}$$

The probe-on-probe sensitivity model (13) was experimentally validated. Table 1 shows the validation results for three probe-on-probe tests where the average of these results shows < 1% of error between the experiments and 13.

5. ADHESION FORCE

At adhesion, exactly at the instance before the probes' separation from each other, the adhesion force between the probes could be found experimentally from jump-off-contact (JOC) deflection, as shown in Figure 6. On the other hand, the pull-off force could be calculated from Johnson, Kendall, and Roberts (JKR) model [6], also from Derjaguin, Muller, and Toporov (DMT) model [7].

Table 1. Validation of probe-on-probe sensitivity equation for three tests.

Test	$\frac{\partial V_1}{\partial x_{Cb}}$	a_1	$\frac{\partial V_2}{\partial x_{Cb}}$	a_2		Validation	error
1	-0.81	-0.78	0.0246	-1.57		1.023	+2%
2	-0.81	-0.779	0.026	-1.456		1.022	+2%
3	-0.79	-0.81	0.025	-1.46		0.958	-4%
Avg.	-0.8	-0.79	0.0252	-1.462		0.9954	<1%

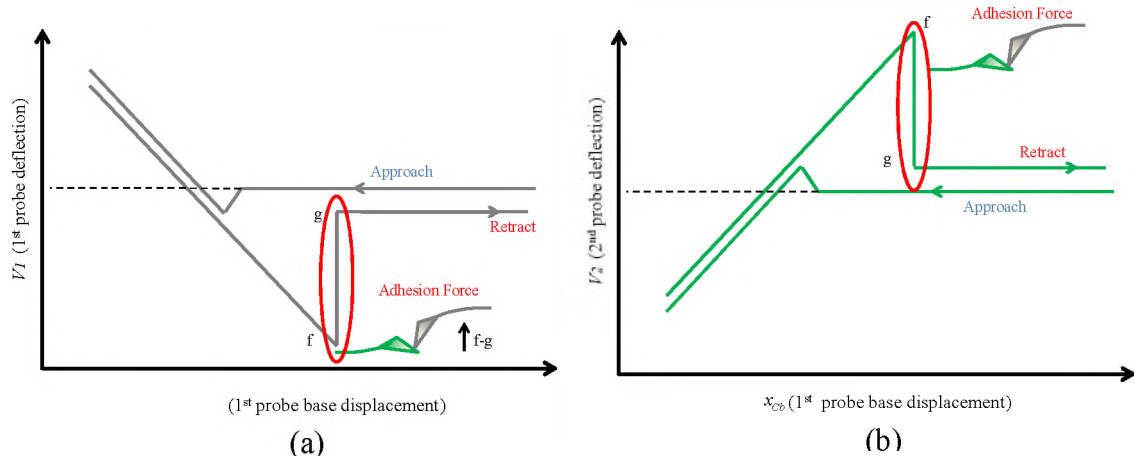

Figure 6. (a) Probe-on-probe adhesion force of 1st probe. (b) Probe-on-probe adhesion force of 2nd probe.

The adhesion force models F_{adh}^{DMT} and F_{adh}^{JKR} represent the range over which the experimental adhesion force may vary for elastic and non-elastic models [3],

$$F_{adh}^{DMT} = -2\pi R\omega_{ikj} \tag{15}$$

$$F_{adh}^{DMT} = -\frac{3}{2}\pi R\omega_{ikj} \tag{16}$$

$$\omega_{ikj} = 2\gamma \tag{17}$$

where ω_{ikj} is the work of adhesion between the two surfaces i and j in a medium k, γ is a surface energy, and R is tip radius in nm.

5.1. ADHESION FORCE VALIDATION

The adhesion force was experimentally measured from probe-on-probe interaction where the 1st and 2nd probes were silicon probes with a stiffness of k_C=0.3675 and

k_T =27.1 nN/nm respectively. For a silicon probe, the surface energy was $\gamma = 1240$ mJ/m^2, and the adhesion force was calculated from (15) and (16):

$$F_{adh}^{DMT} = 2\pi R\omega_{ikj} = 68.2 \text{ nN},$$

$$F_{adh}^{JKR} = \frac{3}{2}\pi R\omega_{ikj} = 63.5 \text{ nN}.$$

Comparing these results with the experimental work shows that the experimental adhesion force is within the range of the calculated force. Table 2 summarizes the probe-on-probe adhesion force for the two experiments.

Table 2. Summarized probe-on-probe adhesion force results for two experiments.

	1st probe		2nd probe		k_C=0.3675		
Test	V_1 mV	a_1	V_2 mV	a_2	k_C/k_T	k_T	Adh. force (nN)
1	89.4	-0.512	3	-1.19	0.014	26.1	63.9
2	95.8	-0.512	3.8	-1.19	0.017	21.5	68.4

6. NATURAL FREQUENCY AT ADHESION

At the adhesion region, when the probes adhere together, the mass and stiffness changed due to adhesion. This change shifts the natural frequency of the probe. For instance, the 2nd probe natural frequency at adhesion is

$$\omega_n = \sqrt{\frac{k_C + k_T}{m_C + m_T}}. \tag{18}$$

From the 1st probe and 2nd probe factory nominal parameters, by using $m = \rho v$ where ρ is density and v is probe volume, found that,

$$m_C = 0.6 m_T . \tag{19}$$

Taking into account that $k_C = 0.367$, which is very small compared with $k_T = 27.2$, and substituting in (15) yields

$$\omega_n = \frac{1}{\sqrt{1.6}} \sqrt{\frac{k_T}{m_T}} = 0.79 \sqrt{\frac{k_T}{m_T}},$$

$$\omega_n = 0.79 \omega_{n1} . \tag{20}$$

Applying (20) to the experimental results show that the error is 2% as shown in Figure (7)

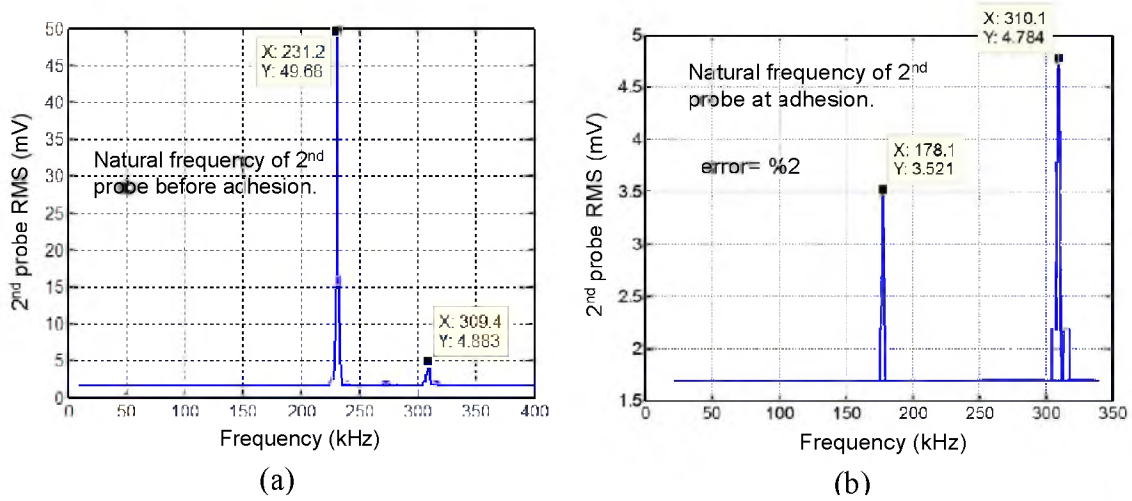

Figure 7. (a) Natural frequency before adhesion. (b) Natural frequency at adhesion.

7. STIFFNESS CALIBRATION USING FREQUENCY SCALING

A spring constant of a rectangular cross section cantilever beam could be found by [4] [5]

$$k = \frac{Et^3 w}{4l^3} \tag{21}$$

where l is beam length, w is the beam width, t is beam thickness, and E is Young's modulus of elasticity. For a cantilever beam with a stiffness k and density ρ the effective mass m_{eff} can be calculated from beam geometry [8] [9]:

$$m_{eff} = 0.24m \tag{22}$$

where $m = \rho lwt$ is the beam mass from geometry.

Assuming, a cantilever beam has a natural frequency f_0, then

$$f_0 = \frac{\omega}{2\pi} = \frac{1}{4\pi l^2}\left(\frac{E}{0.24\rho}\right)^{1/2} \approx \frac{1}{2\pi l^2}\left(\frac{E}{\rho}\right)^{1/2}. \tag{23}$$

We could rewrite (21) using (23) and yields

$$k \approx 2\pi^3 l^3 f_0^3 w\sqrt{\rho^3/E} \tag{24}$$

Eqnuation (24) shows that the cantilever stiffness is proportional to natural frequency. This provides a simple method to calibrate AFM probe stiffness based on natural frequency.

For a silicon probe, Young's modulus of elasticity is $E = 186.5$ GPa and density is $\rho = 2330$ kg/m^3. For the 1st probe, the natural frequency was experimentally measured by means of frequency sweeping and was found to be $f_0 = 17.205$ kHz. The probe dimension was length $l = 450$ μm, and width the $w = 50$ μm. The 2nd probe stiffness k_C was found from (24):

$$k_C = 0.367 \text{ N/m}.$$

For 2nd probe, natural frequency $f_0 = 231.96$ kHz, length $l = 140$ μm, and width $w = 50$ μm. 2nd probe stiffness k_T found from (24)

$$k_T = 27.1 \text{ N/m}.$$

stiffness ratio is $\frac{k_C}{k_T} = 0.0136$, also, stiffness ratio validated with probe-on-probe interaction as shown in table (2).

8. CONCLUSIONS

DP-AFM Probe-on-probe interaction investigated using probe-on-probe approach retract curve. Probe-on-probe universal sensitivity model were found and validated with experimental work, the error found to be < 4 %. Probe-on-probe adhesion force found from Jump of contact distance. The adhesion force found to be fall between JKR and DMT model for adhesion force, the reason for that is these models represent the adhesion force for soft and hard material respectively. Also, at adhesion, the natural frequency reduced due to the increase of mass at adhesion, 2nd probe natural frequency modeled and experimentally measured before and during adhesion, the results show that 2nd probe natural frequency reduced due to the increase of the mass due to adhesion, the error between the modeled and experimental natural frequency at adhesion found to be 2%.

ACKNOWLEDGEMENTS

This work is supported by National Science Foundation, CMMI-1229701.

REFERENCES

[1] Binnig, G., Quate, C., and Gerber C., "Atomic Force Microscope," *Physical Review Letters*, Vol. 56(9), pp. 930-933, 1986.

[2] Mokaberi, B., and Requicha, A. A., "Drift compensation for automatic nanomanipulation with scanning probe microscopes," *IEEE Transactions on Automation Science and Engineering*, *3*(3), pp.199-207, 2006.

[3] Israelachvili, J., "Intermolecular and Surface Forces," Boston, MA, Academic Press, 1985.

[4] Loganathan, M., Al-Ogaidi, A., and Bristow, D., "Design and Control of Dual-Probes Atomic Force Microscope" IEEE/ASME Transaction on Mechatronics, Vol. 23 Issue 1, pp 424-433 Feb. 2018.

[5] Tsunemi, E., et. al., "Development of Multi-Environment Dual-Probe Atomic Force Microscopy System Using Optical Beam Deflection Sensors with Vertically Incident Laser Beams," *Review of Scientific Instruments*, Vol. 84(8), pp. 083701: 1-7, 2013.

[6] Johnson, K. L., Kendall, K., and Roberts, A. D., " Surface Energy and the Contact of Elastic Solids," Proceedings of the Royal Society of London. Series A, Mathematical and Physical Sciences, Vol. 324, No. 1558 (Sep. 8, 1971), pp. 301-313.

[7] Derjaguin, B. V., Muller, V. M., and Toporov, Yu. P., "Effect of contact deformations on the adhesion of particles," *In Journal of Colloid and Interface Science*, Volume 53, Issue 2, 1975, Pages 314-326.

[8] Cleveland, J. P., and Manne, S., "A Nondestructive Method for Determining the Spring Constant of Cantilevers for Scanning Force Microscopy," *Rev. Sci. Instrum.* 64 (2) Feb. 1994.

[9] Ohler, B., "Cantilever Spring Constant Calibration Using Laser Doppler Vibromety," *Rev. Sci. Instrum.* 78, 2007.

[10] Al-Ogaidi, A., and Bristow, D., "Uniform Ultimate Boundedness of Probe-to-Probe Dynamics in Dual Probes Atomics Force Microscopy," *Proceedings of ASME 2014 Dynamic Systems and Control Conference*, San Antonio, Texas, Oct. 22-24, 2014.

II. ITERATIVE LEARNING CONTROL OF Z-AXIS NANO STAGE WITH STOCHASTIC NOISE

Ayad Al-Ogaidi and Douglas A. Bristow

ABSTRACT

In this paper, Iterative Learning Control (ILC) for nano positioning stage is examined with four ILC algorithms. The nano stage model was identified using frequency response of the stage. Deterministic and stochastic noise spectrum was identified experimentally. Optimal Q filter and learning filter (L -filter) designed depending on the deterministic and stochastic noise spectrum. The error norm experimentally found to be converging for all four ILC algorithms.

1. INTRODUCTION

Iterative learning control (ILC) [6]-[8] is a control process used for systems with repetitive operation. It also used to improve the performance of the system and tracking error from iteration to iteration to generate a control signal for the next iterations.

The ILC considered for the system which repeat the same operation again and again under the same initial conditions. For this kind of system, the error contains good information about system behavior from one iteration to another. The ILC incorporates this information to generate the feedforward input signal for the next iteration.

One of the advantages of the ILC over the feedback and feedforward controller is the way to response for noise and disturbance. Feedback controller response to the reference input and disturbance which causing lag in the response. Feedforward controller

compensate for disturbance with known reference signal. However this not the case for the ILC, the ILC use the information from the previous iteration to compensate for repeating disturbance.

Despite the input signal is always corrupted with noise, most of the ILC work assumes it is noise free. However, this is not the case in practical implementation. To better compensate for the noise and disturbances, knowledge of the noise and disturbance spectrum could be used for the generation of the ILC input.

The rest of this paper is organized as follow, Section 2 represent the procedure and calculation required for the ILC implementation. Section 3 represent the different ILC algorithms. Section 4 represents the experimental and simulation work. Section 5 contains the conclusion and future work.

2. ILC CALCULATIONS

Consider the following error model for a motion system as,

$$e_j(k) = -P(z)u_j(k) + d(k) + w_j(k) \tag{1}$$

where $d(k)$ is a deterministic disturbance, and $w_j(k)$ is a stochastic disturbance of j at the is the discrete time sample k, and $P(z)$ is a stable close loop plant. Consider the ILC control input law u is,

$$u_{j+1}(k) = Q(z)(u_j(k) + L(z)\hat{e}_j(k)) \tag{2}$$

where $\hat{e}_j(t)$ is a noise corrupted error measurement modeled as

$$\hat{e}_j(k) = e_j(k) + v_j(k) \tag{3}$$

and $v_j(t)$ is stationary random noise. The ILC block diagram is shown at Figure 1.

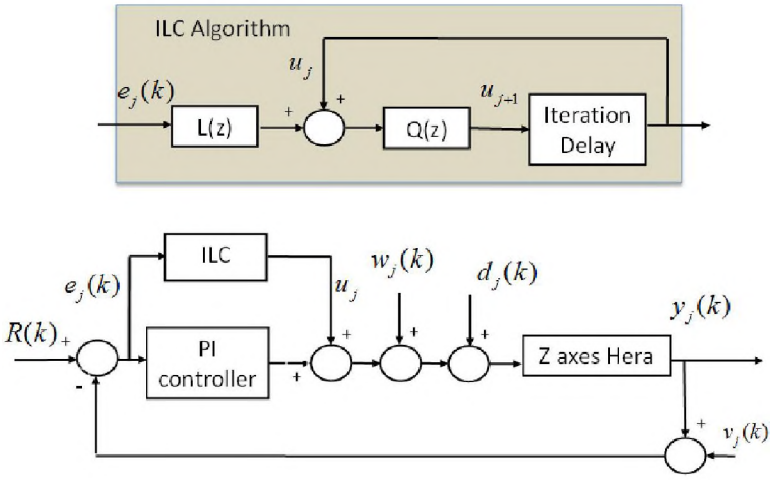

Figure 1. ILC block diagram.

3. SYSTEM IDENTIFICATION AND NOISE MODELING

3.1. NANO STAGE MODEL

Nano stages are an integral part of nanotechnology instruments. They offer sub-nanometer precision over several microns range. They are often used in atomic force microscopy (AFM) [1], where sub-nanometer positioning and accuracy are critical. Figure 2 shows a piezo-based nano stage (PI P-620.ZCL) on which the proposed ILC scheme was applied. The stage has a travel range of 50 µm and 0.1 nm resolution.

A linear model for the nano stage was identified using the frequency response of the stage shown in Figure 3.

The transfer function of the fitted model is given in (4),

$$G(s) = \frac{k_z(s^2 + 2\xi_1\omega_2 s + \omega_2^2)}{(s+\omega_1)(s^2 + 2\xi_2\omega_2 s + \omega_2^2)(s^2 + 2\xi_3\omega_3 s + \omega_3^2)} \tag{4}$$

where $k_z = 2.5028*10^{10}$, ω_1=1000, ω_2=5282, ω_3=6978 (rad/sec), $\xi_1 = 0.025$, $\xi_2 = 0.3$,

and $\xi_3 = 0.1$. Further, for implementation the system model G(s) is discretized with sampling rate of 12500 samples/sec as in (5),

$$G(z) = \frac{0.00189(z+3.29)(z+0.25)(z^2-1.81z+0.98)}{(z-0.92)(z^2-1.62z+0.78)(z^2-1.6z+0.89)}. \quad (5)$$

Figure 2. PI-Hera Nano stage (P-620.ZCL) with travel range of 50 µm.

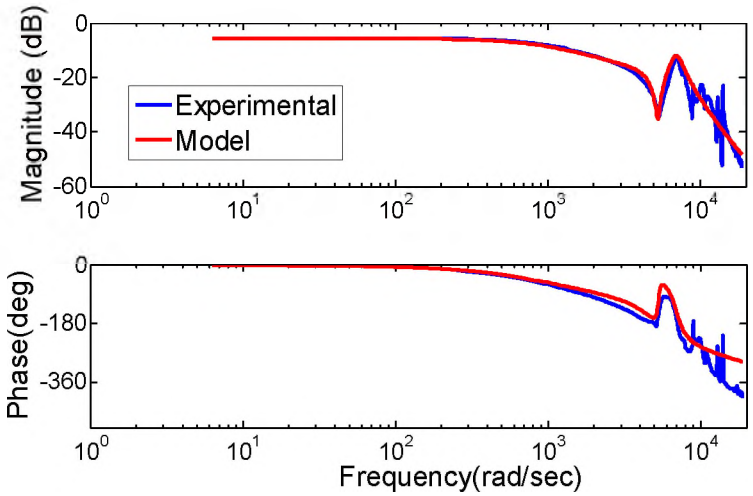

Figure 3. Experimental frequency response and the fitted model of the nano stage.

3.2. DETERMINISTIC AND STOCHASTIC NOISE SPECTRUM

The nano stage is controlled with a discrete PI controller $C(z)$ with proportional gain $k_p = 0.06$, and integral gain $k_i = 45$ as in (6).

$$C(z) = k_p + \frac{k_i dt}{z-1} \tag{6}$$

where 1/dt is the sampling rate. For implementation the controller is discretized as C(z) with sampling rate 12500 samples/sec.

To obtain the stochastic and deterministic noise model, a number of zero input signals were applied to (1), and the error signals were measured. Hence (3) becomes,

$$\hat{e}_j(k) = d(k) + w_j(k) + v_j(k) \tag{7}$$

Since the nano stage is installed on a vibration isolation table to prevent it from ground vibrations and disturbances, it can be safely assumed that the disturbance $w_j = 0$ for all j. This in turn implies that the stochastic disturbance spectrum, $\phi_w(\omega) = 0$. Then (7) becomes,

$$\hat{e}_j(k) = d(k) + v_j(k) \tag{8}$$

and when a number of zero input signals are applied,

$$\sum_{j=1}^{N} \hat{e}_j(k) = \sum_{j=1}^{N} d(k) + \sum_{j=1}^{N} v_j(k). \tag{9}$$

As $N \to \infty$, $\sum_{j=1}^{N} v_j(k) = 0$, and

$$\sum_{j=1}^{N} e_j(k) = Nd(k)$$

So,
$$d(k) \approx \frac{1}{N} \sum_{j=1}^{N} e_j(k). \tag{10}$$

So the measurements noise can be obtained as,

$$v_j(k) \simeq \hat{e}_j(k) - d(k) \tag{11}$$

using the definition of Fourier transform, the stochastic noise spectrum can be written as,

$$\phi_v(\omega) = \frac{1}{N}\sum_{j=1}^{N}\left|FFT[v_j(k)]\right|^2. \tag{12}$$

Similarly the deterministic spectrum can be represented as,

$$\phi_d(\omega) = \left|FFT[d(k)]\right|^2. \tag{13}$$

An experiment was carried out by applying zero input signal for N=400 iterations, and the measured error signal was used to calculate the experimental deterministic and stochastic noise spectrum using (12) and (13). Figure 4 shows the stochastic noise spectrum ϕ_v, and implementing (13) result in experimental deterministic spectrum. Mathematically the deterministic signal can be written as,

$$d(k) = \frac{1}{1+C(z)G(z)}r(k) \tag{14}$$

where $r(k)$ is the reference signal (1nm smooth square wave), shown in Figure 5. The experimental and theoretical deterministic spectrum is shown in Figure 6. As seen in the Figure 6 the experimental and mathematical deterministic spectrum are matching at low frequencies (<100 Hz), while the experimental deterministic spectrum corrupted with noise at high frequencies (≥100) due to measurements noise. However, this noise level decrease as the number repetitions, N increases, which in turn makes the experimental converge the theoretical. So, for the calculation of optimal Q and L filter (14) will be used.

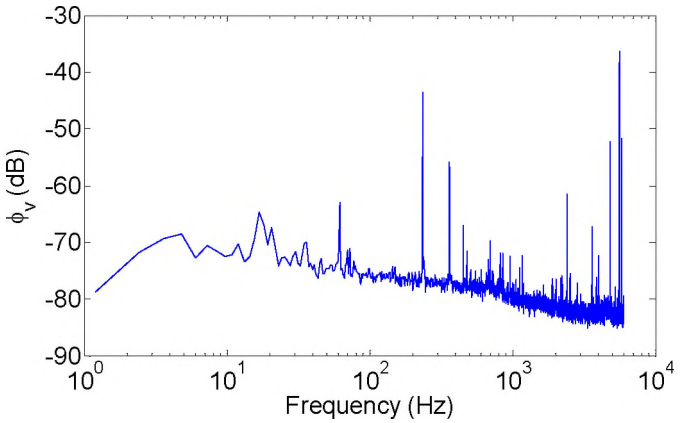

Figure 4. Experimental stochastic measurement noise spectrum.

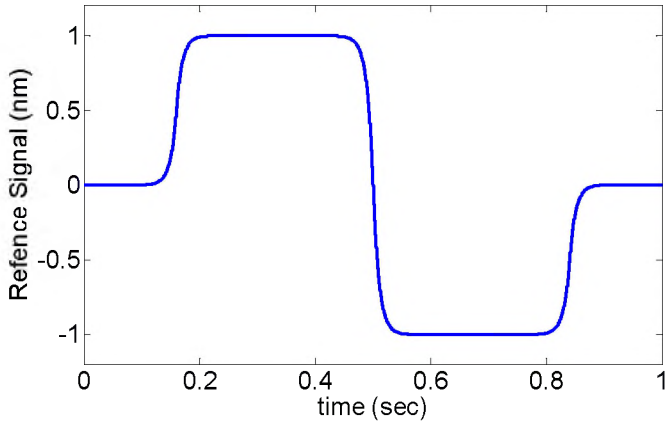

Figure 5. Reference signal.

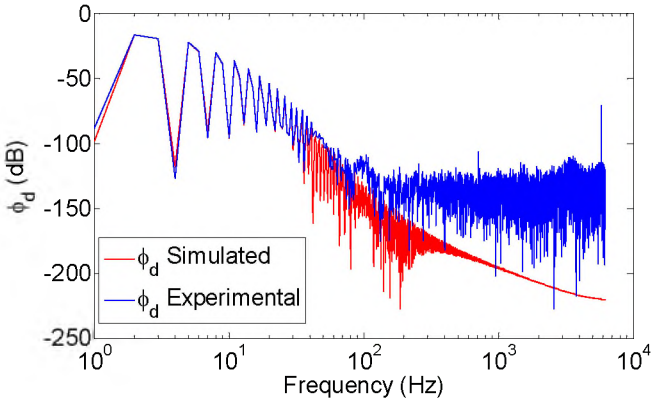

Figure 6. Deterministic noise spectrum.

The deterministic-to- stochastic ratio (*DSR*) is defined as,

$$DSR(\omega) = \frac{\phi_d(\omega)}{\phi_w(\omega) + \phi_v(\omega)} \tag{15}$$

The *DSR* plays a role in learning for stochastic type ILC. At low frequencies the *DSR* is large and the stochastic noise is very small, thus the learning could be fast. At high frequencies where the DSR is small, the deterministic error is very small such that there is little benefit in learning those frequencies. and the deterministic error will be learned very slowly [2-3].

3.3. ZERO PHASE TRACKER

The zero phase tracker [5] method is used to realize a stable learning filter when the plant is non-minimum phase. If the plant is minimum phase, then the learning filter is designed by inverting plant transfer function as,

$$L(z) = H\hat{P}^{-1}(z) \tag{16}$$

where H is the learning gain. When the plant is nonminimum phase, then inverting the plant it will yield an unstable learning filter. To overcome this issue the learning filter is obtained as follows.

Let $\hat{P}$ be the closed loop plant, so

$$P(z) = \frac{G(z)}{1 + G(z)C(z)} \tag{17}$$

Rewrite (17) as,

$$P(z) = \frac{B^-(z)B^+(z)}{A^-(z)} \tag{18}$$

where $B^{-}(z)$ and $B^{+}(z)$ represent the stable and unstable zeros respectively, and $A^{-}(z)$ represents the stable poles.

Let $b \geq \left\| B^{+}(z) \right\|_{\infty}^{2}$. As per zero phase tracker method, a stable learning filter can be designed as,

$$L(z) = \frac{H}{b} \frac{A^{-}(z) B^{+}(z^{-1})}{B^{-}(z)}, \tag{19}$$

where H is a learning gain.

For the nano stage $G(z)$, P is given by,

$$P(z) = \frac{0.0019(z-1)(z+0.24)(z^2-1.8z+0.98)(z+3.29)}{(z-0.99)(z-0.9)(z^2-1.6z+0.77)(z^2-1.6z+0.9)}. \tag{20}$$

Applying the zero phase tracker method to find a stable learning filter,

$$L(z) = H \frac{94.27(z-0.99)(z-0.9)(z+0.3)(z^2-1.6z+0.8)(z^2-1.61z+0.9)}{z(z+0.25)(z-1)(z^2-1.8z+0.98)}$$

$L(z)$ has to have at least zero relative degree (causal) to implement it in real time. To make $L(z)$ with zero relative degree, let $L_{new}(z) = z^{-m} L(z)$ where m is the relative degree. Then,

$$L_{new}(z) = H \frac{94.27(z-0.99)(z-0.9)(z+0.3)(z^2-1.6z+0.8)(z^2-1.6z+0.9)}{z^3(z+0.25)(z-1)(z^2-1.8z+0.98)} \tag{21}$$

The effect of making $L(z)$ with zero relative degree has to be compensated by advancing the error by *m* samples as,

$$L(z)\hat{e}_j(k) = z^{-m} L(z)\hat{e}_j(k) z^m = L_{new}(z)\hat{e}_j(k) z^m = L_{new}(z)\hat{e}_j(k+m)$$

which can be accomplished because the entire error history, $e_j(k)$, $k = 0,...,N-1$ is known during the learning calculation. To avoid shortage of error data, $n+m$ error samples have to be collected instead of n samples.

4. ILC ALGORITHMS

4.1. HEURISTIC ITERATION INVARIANT ILC (*HII*)

The heuristic iteration invariant ILC represented by[4],

$$Q_j(z) = 1, \tag{22}$$

$$L(z) = H\hat{P}^{-1}(z), \tag{23}$$

$$H = k_r, \tag{24}$$

$$u_{j+1} = Q_s(z)Q(z)(u_j + L(z)\hat{e}_j), \tag{25}$$

where k_r is learning gain, $0 < k_r \le 1$. $Q_s(z)$ is a stabilizing filter.

4.2. STOCHASTIC ITERATION INVARIANT ILC (*SII*)

For the stochastic Iteration invariant ILC, the learning filter and Q filter are [2],

$$Q_{opt}(\omega) == \frac{(1+\gamma)\phi_d(\omega) + \gamma(1-\gamma)(\phi_w(\omega) + \phi_v(\omega))}{(1+\gamma)\phi_d(\omega) + (1-\gamma)(\phi_w(\omega) + \phi_v(\omega))}, \tag{26}$$

$$L_{opt}(\omega) = H(\omega)\hat{P}^{-1}(\omega), \tag{27}$$

$$H(\omega) = \frac{(1-\gamma^2)\phi_d(\omega)}{(1+\gamma)\phi_d(\omega) + \gamma(1-\gamma)(\phi_w(\omega) + \phi_v(\omega))}, \tag{28}$$

$$u_{j+1}(\omega) = Q_s(e^{i\omega})Q_{opt}(\omega)(u_j(\omega) + L_{opt}(\omega)\hat{e}_j(\omega)) \tag{29}$$

where γ is the convergence rate.

4.3. HEURISTIC ITERATION VARYING ILC (*HIV*)

The heuristic iteration Varying ILC is [4],

$$Q_j(z) = 1, \tag{30}$$

$$L_j(z) = H_j \hat{P}^{-1}(z), \tag{31}$$

$$H_j = \frac{1}{1+j}, \tag{32}$$

$$u_{j+1} = Q_s(z)Q_j(z)(u_j + L_j(z)\hat{e}_j), \tag{33}$$

4.4. STOCHASTIC ITERATION VARYING ILC (*SIV*)

The stochastic iteration varying ILC is [3],

$$Q_j(e^{j\omega}) = 1, \tag{34}$$

$$L_j(e^{j\omega}) = H_j(\omega)\hat{P}^{-1}(e^{j\omega}), \tag{35}$$

$$H_j(\omega) = \frac{\eta(\omega)}{(1+j)\eta(\omega)+1}, \tag{36}$$

$$u_{j+1}(\omega) = Q_s(z)Q_j(e^{j\omega})(u_j(\omega) + L(e^{j\omega})\hat{e}_j(\omega)), \tag{37}$$

5. EXPERIMENTAL RESULTS

The stochastic ILC control scheme was implemented to control the position of a PI-Hera Nano stage (P-620.ZCL). An NI Real time controller (NI-PXIe 8135) was used for control implementation at a sampling rate of 12500 samples/sec. The base line controller was set to PI controller.

Due to the large noise in the system $\|v_j\|_2 = 126$ nm, an accurate instrument have to be used to find the actual error e_j. Instead, an average method will be used to obtain the actual measurement. All experiments have been implemented with 20 learning iteration, and for iteration $j = 0,1,...,10$ and $j = 20$ each iteration averaged for 4000 repetitions to find the actual measurement. As N increases the averaged measurement noise v_j will decrease. So as $N \to \infty$, and the averaged error measurement will converge to the actual error measurement as from (3). The actual error e_j for the j^{th} iteration was calculated as,

$$e_j = \frac{1}{N}\sum_{i=1}^{N} \hat{e}_{j,i} \tag{38}$$

The ILC input implemented with stabilizing filter $Q_s(z)$ where $Q_s(z)$ is a zero phase 10^{th} order chebyshev II low pass filter with bandwidth of 1.4 kHz. $Q_s(z)$ is used to filter unstable frequencies such that the ILC achieve perfect tracking for frequencies were the magnitude of $Q_s(z)$=1, and the ILC is off when the magnitude of the $Q_s(z)$=0. The ILC input update becomes,

$$u_{j+1} = Q_s(z)Q(z)(u_j + L(z)\hat{e}_j)$$

For the Stochastic Iteration Invariant (*SII*) and Stochastic Iteration Varying (*SIV*) ILC, the optimal Q filter and L filter were designed based on the deterministic and stochastic noise models. The convergence rate for *SII* was selected as $\gamma = 0.5$. For heuristic Iteration Invariant (*HII*) the learning gain was selected as $H = 0.5$. The learning was applied each iteration for 20 iterations, where 20 assumed to be large enough to

ensure asymptotic convergence of the error. The tracking error norm $\|e_j\|$ for different ILC schemes is shown in Figure (7). For S*IV* ILC, the $\|e_j\|$ is converging very fast for the first iteration, then it start converging slowly after that. The S*IV* ILC achieves the smallest $\|e_j\|$ among the *HII*, *HIV,* and *SII* ILC with $\|e_j\|= 2.6$ nm as shown in Figure (7). For comparison between stochastic and heuristic, the stochastic ILC reduces the error about 10 times less than the heuristic ILC as shown in figure (7).

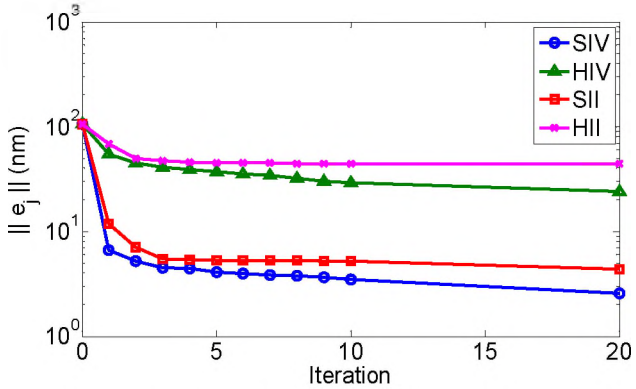

Figure 7 Experimental $\|e_j\|$ for all four ILC.

6. CONCLUSIONS

We have experimentally implemented a frequency domain based ILC (*SII,SIV*) for systems with deterministic and stochastic noise. This ILC scheme guarantees better tracking error convergence irrespective of noise. The optimal Q and L filter designed based on the stochastic and deterministic noise spectrum. Experimentally, the scheme was applied for position control of a nano stage and its performance was compared to heuristic type ILC (*HII, HIV*). The stochastic ILC reduced the tracking error norm $\|e_j\|$ by an order of magnitude compared to heuristic type ILC.

ACKNOWLEDGEMENTS

This work is supported by the National Science Foundation, CMMI-1229701.

REFERENCES

[1] Binnig, G., Quate, C., and Gerber C., "Atomic Force Microscope," Physical Review Letters, Vol. 56(9), pp. 930-933, 1986.

[2] Bristow, D., "Frequency Domain Analysis and Design of Iterative Learning Control for Systems with Stochastic Disturbances." American Control Conference, Washington, USA, 2008.

[3] Bristow, D., "Optimal Iteration-Varying Iterative Learning Control for Systems with Stochastic Disturbances." American Control Conference, Baltimore, MD, 2010.

[4] Butcher, M., Karimi, A., and Longchamp, R., "A Statistical Analysis of Certain Iterative Learning Control Algorithms," International Journal of Control, vol. 81, no. 1, pp. 156-66, 2008.

[5] Tomizuka, M., "Zero Phase Error Tracking Algorithm for Discrete Control", ASME Journal of Dynamic Systems, Measurement and Control. Vol 109 (1), pp. 65-68. 1987.

[6] Moore, K.L., "Iterative Learning Control for Deterministic Systems," Springer-Verlag, 1993.

[7] Bien, Z. and J.-X. Xu, "Iterative Learning Control: Analysis, Design, Integration and Applications," Kluwer Academic Publishers, 1998.

[8] Bristow, D.A., M. Tharayil, and A.G. Alleyne, "A Survey of Iterative Learning Control," IEEE Control Systems Magazine, vol. 26, no. 3, pp. 96-114, 2006.

[9] Saab, S.S., "A Discrete-Time Stochastic Learning Control Algorithm," IEEE Trans. on Automatic Control, vol. 46, no. 6, pp. 877-887, 2001.

[10] Saab, S.S., "On a Discrete-Time Stochastic Learning Control Algorithm," IEEE Trans. on Automatic Control, vol. 46, no. 8, pp. 1333-1336, 2001.

[11] Saab, S.S., "Stochastic P-Type/D-Type Iterative Learning Control Algorithms," International J. of Control, vol. 76, no. 2, pp. 139-148, 2003.

[12] Saab, S.S., "Optimal Selection of the Forgetting Matrix into an Iterative Learning Control Algorithm," IEEE Trans. on Automatic Control, vol. 50, no. 12, pp. 2039-43, 2005.

SECTION

2. CONCLUSIONS

In Paper I, dynamics of probe-on-probe interaction force of DP-AFM were linearized into three regions: no interaction, attraction region, and repulsion region. This linearized interaction force model led to a state-dependent switching system model of three subsystems. Stability of every subsystem was established using Lyapunov stability theorem and proven to be UUB. However, the ultimate bound was found to be conservative, and this will be addressed in future work. Sequence nonincreasing condition proposed in Corollary (1) was employed to ensure the convergence of every subsystem at the switching surface, which satisfies the convergence of the switched system. The results show that a stable probe-on-probe interaction can be determined for a range of probe dynamics within the operation region.

In Paper II, statics of probe-on-probe interaction was investigated using the probe-on-probe approach-retract curve. A probe-on-probe universal sensitivity model were found and validated with experimental work. The error was found to be $< 4\%$. Also, at adhesion, the natural frequency was reduced due to the increase of mass at adhesion. Probe-on-probe adhesion force was found from jump-off-contact distance. The adhesion force was found to be fall between JKR and DMT model for adhesion force. The reason for that is these models represent the adhesion force for soft and hard material, respectively.

In Paper III, a frequency-domain based ILC (*SII,SIV*) has been developed for systems with deterministic and stochastic noise. This ILC scheme guarantees better tracking error convergence irrespective of noise. The optimal Q and L filter was designed

based on the stochastic and deterministic noise spectrum. Experimentally, the scheme was applied for position control of a nano stage and its performance was compared to a heuristic-type ILC (*HII, HIV*). The stochastic ILC reduced the tracking error norm $\| e_j \|$ by an order of magnitude compared to heuristic-type ILC.

BIBLIOGRAPHY

[1] G. Binnig and C. F. Quate, "Atomic Force Microscope," *Physical Review Letters*, 56(9), pp. 930-933, 1986.

[2] S. Alexander, L. Hellemans, O. Marti, J. Schneir, V. Elings, P. K. Hansma, M. Longmire and J. Gurley, "An atomic-resolution atomic-force microscope implemented using an optical lever," *Journal of Applied Physics*, *65*(1), pp.164-167, 1989.

[3] N. Jalili and K. Laxminarayana, "A review of atomic force microscopy imaging systems: application to molecular metrology and biological sciences," *Mechatronics*, 14, pp. 907-945, 2004.

[4] I. Tanaka, I. Kamiya, H. Sakaki, N. Qureshi, S. J. Allen Jr and P. M. Petroff, "Imaging and probing electronic properties of self-assembled InAs quantum dots by atomic force microscopy with conductive tip," *Applied physics letters*, *74*(6), pp.844-846, 1999.

[5] R. Garcia and R. Perez, "Dynamic atomic force microscopy methods," *Surface Science Reports*, 47, pp. 197-301, 2002.

[6] A. L. Weisenhorn, P. K. Hansma, T. R. Albrecht and C. F. Quate, "Forces in atomic force microscopy in air and water," *Applied Physics Letters*, *54*(26), pp.2651-2653, 1989.

[7] C. A. Putman, K. O. Van der Werf, B. G. De Grooth, N. F. Van Hulst, and J. Greve, "Tapping mode atomic force microscopy in liquid," *Applied Physics Letters*, *64*(18), pp. 2454-2456, 1994.

[8] S. I. Kitamura, and M. Iwatsuki, "High-resolution imaging of contact potential difference with ultrahigh vacuum noncontact atomic force microscope," *Applied Physics Letters*, 72(24), pp. 3154-3156, 1998.

[9] R. Garcia, and A. San Paulo, "Attractive and repulsive tip-sample interaction regimes in tapping-mode atomic force microscopy," *Physical Review B*, *60*(7), p.4961, 1999.

[10] M. L. Bloo, H. Haitjema and W. O. Pril, "Deformation and wear of pyramidal, silicon-nitride AFM tips scanning micrometre-size features in contact mode," *Measurement*, *25*(3), pp.203-211, 1999.

[11] M. Loganathan, A. Al-Ogaidi, and D. Bristow, "Design and Control of Dual-Probes Atomic Force Microscope," *IEEE/ASME Transaction on Mechatronics, 23(1)*, pp. 424-433, 2018.

[12] B. Mokaberi and A. A. Requicha, "Drift compensation for automatic nanomanipulation with scanning probe microscopes," *IEEE Transactions on Automation Science and Engineering*, *3*(3), pp.199-207, 2006.

[13] A. Al-Ogaidi, and D. Bristow, "Uniform Ultimate Boundedness of Probe-to-Probe Dynamics in Dual Probes Atomics Force Microscopy," *Proceedings of ASME 2014 Dynamic Systems and Control Conference*, San Antonio, Texas, Oct. 22-24, 2014.

[14] K. Moore, "Iterative Learning Control for Deterministic Systems," Springer-Verlag, 1993.

[15] Z. Bien, and J.-X. Xu, "Iterative Learning Control: Analysis, Design, Integration and Applications," Kluwer Academic Publishers, 1998.

[16] D. Bristow, M. Tharayil, and A. Alleyne, "A Survey of Iterative Learning Control," *IEEE Control Systems Magazine, 26(3),* pp. 96-114, 2006.

VITA

Ayad Jasim Mohammed Al-Ogaidi was born in Baghdad, Iraq. He earned his bachelor's degree in Mechatronics Engineering in August 2003 from Baghdad University, Iraq. In October 2003, he joined the Mechatronics Engineering department at Baghdad University. Mr. Al-Ogaidi started his master's degree in Mechatronics Engineering at the same university in November 2005, and earned his master's degree in September 2008. He worked as an assistant instructor in the Mechatronics Engineering Department at the same university from September 2008 to August 2011.

In August 2011, the Higher Committee for Education Developments in Iraq (HCED-Iraq) granted him a scholarship to study his PhD in Mechanical Engineering at Missouri University of Science and Technology. He worked in the Precision Motion Control lab (PMCL) at Missouri S&T under Dr. Douglas Bristow. He received his Ph.D. in Mechanical Engineering in May 2018 from Missouri S&T.